Impact of Incidence Angle Diversity on SMOS and Sentinel-1 Soil Moisture Retrievals at Coarse and Fine Scales

Gerard Portal, *Member, IEEE*, Mercè Vall-llossera, *Senior Member, IEEE*, María Piles, *Senior Member, IEEE*, Thomas Jagdhuber, *Senior Member, IEEE*, Adriano Camps, *Fellow, IEEE*, Miriam Pablos, *Member, IEEE*, Carlos López-Martínez, *Senior Member, IEEE*, Narendra N. Das, *Senior Member, IEEE*, and Dara Entekhabi, *Fellow, IEEE*

Abstract*— Incidence angle diversity of space-borne radiometer and radar systems operating at low microwave frequencies needs to be taken into consideration to accurately estimate soil moisture (SM) across spatial scales. In this study, the single channel algorithm (SCA) is first applied to Soil Moisture and Ocean Salinity (SMOS) brightness temperatures at vertical polarization (TB_V) to estimate SM at coarse resolution (25 km) and develop a land cover-specific and incidence angle (32.5°, 42.5°, and 52.5°)-adaptive calibration of single scattering albedo (ω) and soil roughness (h_s) parameters. These effective parameters are used together with fine-scale multiangular Sentinel-1 backscatter in a single-pass active–passive downscaling approach to estimate TB_V at fine scale (1 km) for each SMOS incidence angle. These TB_Vs are finally inverted to obtain the corresponding high-resolution SM maps. Results over the Iberian Peninsula for year 2018 show an increasing trend of ω and a decreasing trend of h_s with SMOS incidence angle, with almost no variability of ω across land cover types. The active–passive covariation parameter is shown to increase with SMOS incidence angle and decrease with Sentinel-1 incidence angle. Coarse and fine TB_V maps from the three SMOS incidence angles show similar distributions (mean differences below 0.38 K). Resulting high-resolution SM maps have maximum differences in mean and standard deviation of 0.016 and 0.015 m^3/m^3, respectively, and compare well with *in situ* measurements. Our results indicate that model-based microwave approaches to estimate SM can be adequately adapted to account for the incidence angle diversity of planned missions, such as Copernicus Microwave Imaging Radiometer (CIMR), Radar Observing System for Europe in L-band (ROSE-L), and Sentinel-1 next generation.

***Index Terms*— Active–passive microwave, incidence angle, radiometry, signal covariation, spatial disaggregation.**

AQ:1 Manuscript received 12 November 2021; revised 12 February 2022 and 10 May 2022; accepted 6 June 2022. This work was supported in part by AQ:2 MCIN/AEI/10.13039/501100011033 under Project PID2020-114623RB-C32; in part by the Spanish Ministry of Science, Innovation and Universities, through the coordinated project L-Band (MCIU/AEI/FEDER, UE): Sobre la continuidad de las misiones satelitales de banda L. Nuevos paradigmas en productos y aplicaciones, under Grant ESP2017-89463-C3-2-R (UPC part) and Grant ESP2017-89463-C3-1-R (ICM part); and in part by the Unidad de Excelencia María de Maeztu under Grant MDM-2016-0600. The work of María Piles was supported by the Ramón y Cajal Contract under Project RTI2018-096765-A-100 (MCIU/AEI/FEDER, UE). *(Corresponding author: Gerard Portal.)*

Gerard Portal, Mercè Vall-llossera, Adriano Camps, and Carlos López-Martínez are with the CommSensLab, Department of Signal Theory and Communications, and the Institut d'Estudis Espacials de Catalunya (IEEC), Universitat Politècnica de Catalunya (UPC), 08034 Barcelona, Spain (e-mail: gerard.portal@upc.edu).

María Piles is with the Image Processing Laboratory, Universitat de València (UV), 46010 València, Spain.

Thomas Jagdhuber is with the Microwave and Radar Institute, German Aerospace Center (DLR), 82234 Weßling, Germany, and also with the Institute of Geography, University of Augsburg (UniA), 86159 Augsburg, Germany.

Miriam Pablos is with the Institute of Marine Sciences, Spanish National Research Council (ICM-CSIC), 08003 Barcelona, Spain.

Narendra N. Das is with the Department of Biosystems and Agricultural Engineering and the Department of Civil and Environmental Engineering, Michigan State University, East Lansing, MI 48824 USA.

Dara Entekhabi is with the Department of Civil and Environmental Engineering, Massachusetts Institute of Technology, Cambridge, MA 02139 USA.

Digital Object Identifier 10.1109/TGRS.2022.3187467

I. Introduction

OVER the last decades, L-band microwave radiometry has consolidated as the optimal technology to globally estimate surface soil moisture (SM) [1]–[3]. L-band (1–2 GHz) is highly sensitive to SM changes due to high contrast in the permittivity range ($\varepsilon = 3 - 80$) [4]. Moreover, at these frequencies, the atmosphere can be considered nearly transparent, and measurements are less affected by soil roughness and vegetation attenuation than at higher frequencies (e.g., X- or C-bands). Active sensors, in turn, are capable of a higher spatial resolution, but since radar backscatter is highly influenced by surface roughness, vegetation canopy structure, and water content, they have a lower sensitivity to SM under vegetated conditions.

Currently, there are two operational L-band missions, which are devoted to globally map the Earth's SM: the Soil Moisture and Ocean Salinity (SMOS) mission, launched in November 2009; and the Soil Moisture Active Passive (SMAP) mission, launched in January 2015. The SMOS satellite carries the Microwave Imaging Radiometer using Aperture Synthesis (MIRAS), a passive microwave interferometric L-band (1.41 GHz) sensor. This instrument is capable of measuring multiangular (0°–65°) dual polarized—vertical (V) and horizontal (H)—brightness temperatures (TB) of the globe with a revisit time of three days and a spatial resolution of about ~50 km [5]. The SMAP satellite includes a real aperture L-band radiometer (1.41 GHz) and a high-resolution L-band radar (1.26–1.29 GHz), which share a 6-m diameter conical scanning antenna with a surface incidence angle of 40°.

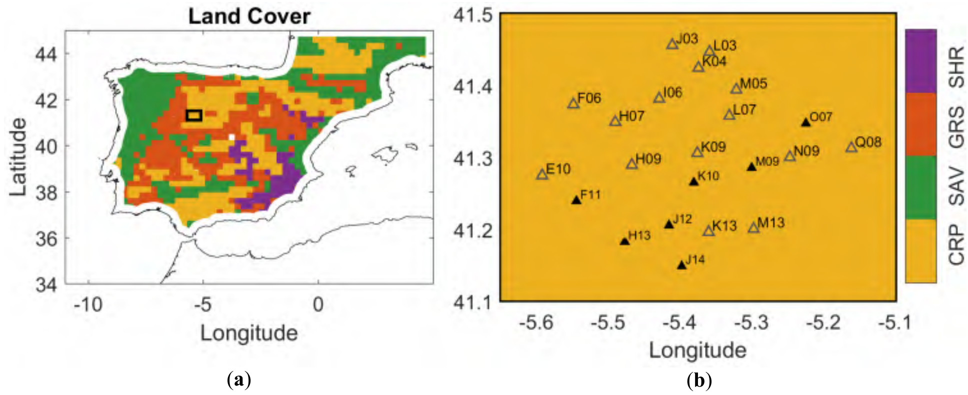

Fig. 1. (a) Classification map of the four most common land cover types over the Iberian Peninsula: croplands (CRP), savannas (SAV), grasslands (GRS), and shrublands (SHR), adapted from MODIS IGBP. The black box marks the location of the REMEDHUS network. (b) Zoom into the region that contains the 22 REMEDHUS validation sites. The location of each of the *in situ* stations is represented by a triangle: filled, for the stations used in this study; or empty, for the rest of the stations that make up the REMEDHUS network.

Although the SMAP radar stopped transmitting in July 2015, its radiometer provides global measures of the Earth's L-band emissivity with a footprint of about 40 km and a revisit time of approximately three days.

Different SM retrieval techniques have been proposed in the context of these two missions. These algorithms differ, for instance, in the TB information they use as an input. Some are designed to exploit one single polarization—single channel algorithm (SCA) with vertical or horizontal polarization ($\mathrm{SCA_V}$ or $\mathrm{SCA_H}$) [6], while others are able to exploit both polarizations jointly—dual channel algorithm (DCA) [7] and land parameter retrieval model (LPRM) [8]. Also, some require time series—multitemporal DCA (MT-DCA) [9]—and others optimize the combined use of multiple incidence angles—official SMOS algorithm from European Spatial Agency (ESA) and SMOS-IC from Institut National de la Recherche Agronomique (INRA) and Center d'Etudes Spatiales de la BIOsphère (CESBIO) [10]. As the abovementioned algorithms, the retrieval techniques introduced in this study are based on the tau-omega ($\tau - \omega$) emission model, a zero-order approximation of the radiative transfer equation. This approximation has been widely used in literature and is currently applied for SM estimation from the SMOS and SMAP surface TB in their baseline algorithms [11]. Also, as shown by Feldman *et al.* [12], the zero-order approximation seems to be sufficient for the Iberian Peninsula, where the predominant IGBP land cover classes are shrublands, savanna, croplands, and grassland (see Fig. 1). In the $\tau - \omega$ model, the emissivity is modeled according to the single scattering albedo (ω) and the vegetation optical depth (τ)—which quantifies the scattering and extinction energy loss in the canopy—the soil roughness (h_s) and the soil temperature (T_S), among other parameters [see (1)] [13]. The accuracy of these parameters is crucial in order to obtain the best possible SM estimates, and hence, several studies have been dedicated to find the optimal parameters' values; in [14], Van der Schalie *et al.* applied the LPRM on SMOS observations to retrieve the optimal ω and h_s values at three independent incidence angles (45°, 52.5°, and 60°). They obtained best results by averaging the retrievals from the three incidence angles, with good agreement with *in situ* over OzNet sites in Australia ($R > 0.7$) and with the SMOS SM L3 product ($R > 0.8$). A similar analysis, but on a global scale, was also carried out by Van der Schalie *et al.* [15], where the resulting estimated SM showed correlations higher than 0.74, in average (considering whole Australia, the Sahel, and large parts of North and South America), when compared against SMOS SM L3. In [16], Fernandez-Moran *et al.* calibrated ω and h_s in the SM retrieval from SMOS observations (considering all incidence angles between 20° and 55°) using the L-band microwave emission of the biosphere (L-MEB) model. They carried out two analyses, one considering globally constant values of ω and h_s and the other considering land cover-dependent values, and reported good correlations ($R > 0.6$) in both cases against *in situ* SM measurements. Other relevant studies focused on the calibration of the parameters involved in the $\tau - \omega$ model can be found in literature (e.g., [9], [17], [18]).

In previous studies, the benefits of incidence angle diversity on SM retrievals have been demonstrated, such as offering the possibility of better constraining the retrieval in the presence of vegetation or of reducing the impact of radio frequency interference (RFI) [19]. Being aware that future passive microwave missions may rely on single-angle acquisition [e.g., Copernicus Microwave Imaging Radiometer (CIMR)], the first objective of the present study is to develop a land cover-specific and incidence angle (32.5°, 42.5°, and 52.5°)-adaptive parametrization of ω and h_s. To do this, the $\mathrm{SCA_V}$ is used to independently obtain the SM maps at 32.5°, 42.5°, and 52.5° to finally analyze their similarities. The second objective is to assess the impact of incidence angle adaptive parametrizations on active–passive TB disaggregation capabilities.

It is widely acknowledged that the coarse resolution of SMOS and SMAP SM maps limits their applicability to develop local and regional applications. Due to the strong demand for satellite-based SM in regional applications, much effort has been devoted to downscaling of the existing coarse-resolution SM datasets to 1 km [20]–[22], hundreds of meters [23] or even tens of meters [24], and to the estimation of high spatial resolution SM from active microwave sensors, e.g., Sentinel-1 [25]–[29].

TABLE I
SUMMARY OF THE APPLIED DATASETS IN THIS STUDY

Source	Variable	Product	Version	Spatial Frequency	Temporal Frequency	Availability
SMOS	*SM*	BEC SMOS L3	3	25 km	Daily	[45]
	TB	BEC SMOS L3	-	25/12.5 km	Daily	*
SMAP	τ	SMAP L2E	4	9 km	Daily	[46]
		SMAP L2 AP1	3	1 km	Daily	[46]
	T_s	SMAP L2E	4	9 km	Daily	[46]
		SMAP L2 AP1	3	1 km	Daily	[46]
	VWC	SMAP L2 AP1	3	1 km	Daily	[46]
	σ	SMAP L2 AP1	3	1 km	Daily	[46]
	CF	SMAP L4 LMC	5	9 km	Static	[46]
MODIS	*LC*	MCD12Q1	6	500 m	Annually	[47]
ECMWF	*SM*	ERA5-land	-	9 km	Hourly	[48]
REMEDHUS	*SM*	REMEDHUS	-	*In situ*	Hourly	[49]
	Precipitation	REMEDHUS	-	*In situ*	Hourly	**

* BEC SMOS L3 data have been directly provided by the Barcelona Expert Center. **Rainfall data have been directly provided by the Water Resources Research group of the University of Salamanca.

Existing SM downscaling techniques can be classified according to the nature of the scaling model (e.g., machine learning-based [30]–[33], semi-empirical [21], and physical [34]) and depending on the input of ancillary data (e.g., microwave/optical [21], [35], [36], microwave active–passive [37], [38], topography [39], and so on) [40]. This study focuses on the specific TB disaggregation technique developed by Das *et al.* [22], which blends passive and active information to disaggregate the SMAP observations, ultimately leading to high-resolution SM retrievals. This downscaling technique is based on the active–passive microwave covariation parameter (β), modeled as a ratio of emission (radiometer) over backscatter (radar) loss terms [41], [42]. Then, the $\mathrm{SCA_V}$ is used to retrieve the SM from the disaggregated TB_V.

The results of this study are relevant in the light of upcoming missions, such as the CIMR that is planned to operate at a constant incidence angle of 55°, the Radar Observing System for Europe in L-band (ROSE-L) planned to work at 25°–46° incidence angles or Sentinel-1 Next Generation. They would benefit from this land cover- and incidence angle-adaptive parametrization and SM retrieval technique, to obtain high-resolution SM maps, providing enhanced continuity to SMOS and SMAP L-band observations.

The study region and the data used in this work are presented in Section II. Section III details how: 1) the $\mathrm{SCA_V}$ algorithm is applied to SMOS TB to calibrate ω and h_s parameters. This analysis is carried out at three incidence angles ($\theta = 32.5°$, $\theta = 42.5°$, and $\theta = 52.5°$) and for four main land cover types (croplands, savannas, grasslands, and shrublands) across the Iberian Peninsula for the year 2018; 2) the active–passive disaggregation technique proposed by Das *et al.* [22] and Jagdhuber *et al.* [41] is adapted to exploit SMOS TB_V and Sentinel-1 data. The adapted algorithm was applied to retrieve SMOS TB_V at high resolution (1 km) for each different angle; and 3) the $\mathrm{SCA_V}$ is applied to retrieve SM at high resolution. Note that since Sentinel-1 only measures VV + VH polarizations over land, only disaggregated SMOS TB at vertical polarization can be obtained with the downscaling approach proposed in this study (Section III-C). Hence, the subsequently shown analyses focus on the vertical polarization. The results are presented and discussed in Section IV. Finally, Section V summarizes the main conclusions and provides perspectives from this study.

II. Test Area and Data Description

All data used in this study cover the Iberian Peninsula (34°–45° N, −11°–5° W) for the year 2018. The coastal areas were discarded to screen out the effect of sea-land contamination [43]. All the data used through the study are summarized in Table I.

A. Iberian Peninsula Area

The Iberian Peninsula covers an area of 583 832 km^2 (34°–45° N, −11°–5° W). Its topography has an average altitude of 600 m due to the vast plateau, known as the Meseta, which is surrounded by several mountain ranges (Cantabrian Mountains, Pyrenees, Central System, Betic System, and Iberian System). The mountain system running from west to east influences the continental climate, blocking banks of moist air from the Atlantic Ocean that could temper inland temperatures.

While a continental climate predominates in inland areas of the Iberian Peninsula with very cold winters (between 0 °C and 3 °C) and hot summers (24 °C in average), in coastal areas, the climate is milder, with an average annual temperature between 16 °C and 18 °C.

In terms of precipitation, three main regions can be distinguished: the north and northwest region, with an annual precipitation exceeding 600 mm (occasionally reaching 2000 mm); the southeast, a semiarid region with annual precipitation below 300 mm; in the rest of the Peninsula, the annual precipitation is less than 600 mm (predominantly dry).

The wet regions of the Peninsula (north and northwest) are mainly dominated by evergreen trees and grasslands, while at the Mediterranean areas, shrublands and xerophilic plants prevail, along with woodlands (holm oak, Aleppo pine, African palm, and Australian eucalyptus). Over the most arid areas, holm oaks have been replaced by thorny bushes [44].

B. Datasets

1) SMOS Data: Two specific SMOS Level 3 (L3) TB products were produced by the Barcelona Expert Center (BEC) on remote sensing to be used in this study. They were obtained by quality filtering the operational ESA SMOS Level 1 (L1) C TB product, using only measurements that are not affected by any RFI (neither center nor tails). Resulting data were corrected by the geometry of the antenna plane, the Faraday rotation due to the ionosphere, and the atmospheric effects. Later, they were linearly interpolated to the selected incidence angles (32.5°, 42.5°, and 52.5°) by least squares using all observations in a range of ±5° with respect to the desired angle and gridded into a 25- and 12.5-km Equal-Area Scalable Earth Grid, Version 2.0 (EASEv2) by a simple average. In the maps at 12.5 km, pixels with data gaps within the orbit swath were filled with an inverse-distance weighting interpolation of TB values at a distance lower than 2 pixels. The obtained daily maps contain the surface TB at vertical and horizontal polarization at the three angles.

The BEC SMOS L3 SM product is obtained by filtering and binning ESA SMOS Level 2 (L2) SM, producing daily SM maps in a 25-km EASE2v2 grid by a weighted average. Filtering comprises discarding grid points with failed retrievals (“no product” flag), affected by RFI (“probability of RFI” flag), without geophysical sense (“out of range” flag), or with a data quality index (DQX) value greater than 0.07 m^3/m^3. [50].

2) Sentinel-1 Data: Sentinel-1A was launched on April 3, 2014, and Sentinel-1B on April 25, 2016. These satellites carry a C-band (5.405 GHz) synthetic aperture radar (SAR) operating in four modes: strip map, interferometric wide (IW) swath, extrawide swath, and wave mode. Sentinel-1 has multiple incidence angles (20°–45°) within the swath and provides dual polarization capability (VV + VH over land).

This study uses data from the SMAP/Sentinel-1 L2 Radiometer/Radar 30-Seconds Scene 3-km EASE-Grid Soil Moisture, Version 3 (SPL2SMAP_S) product. The SPL2SMAP_S product contains estimates of the land surface conditions obtained by combining passive SMAP ascending and descending half-orbit passes and active information from the Sentinel-1A and -1B SAR [51]. In this research, we employed the IW swath mode within the SPL2SMAP_S product of the Sentinel-1 A/B backscatter in co- and cross-polarization at 1-km EASEv2 grid, which was already preprocessed and filtered as detailed in [22].

3) Calibration/Validation Data: The fifth generation of the European ReAnalysis (ERA5-land) is a dataset obtained through global high-resolution numerical integrations of the European Centre for Medium-Range Weather Forecasts (ECMWF) land surface model driven by the downscaled meteorological forcing from the ERA5 climate [52]. ERA5-land describes 53 variables related to the water and energy cycles over land, with global coverage at a spatial resolution of 9 km, providing hourly information for the period from 1981 to present. In this study, we use the ERA5-land volumetric soil water content at 6:00 h local time of the soil layer 1 (0–7 cm).

The Soil Moisture Measurements Station Network of the University of Salamanca (REMEDHUS) [53] is an SM *in situ* network located in the central semiarid area of the Duero Basin, in Spain. This is a nearly flat region, where a continental semiarid Mediterranean climate predominates. The land is mainly cultivated with rainfed cereals, although patchy areas of forest-pasture, irrigated crops, vineyards, and fallow can also be found. The REMEDHUS network is composed of 22 stations equipped with Hydra Probes that provide hourly SM measurements [54] and four automatic weather stations that measure precipitation, air temperature, relative humidity, wind speed, and solar radiation. *In situ* SM measurements are performed at different soil depths, but in this study, we exclusively use the topsoil data at 5 cm depth [49] and the daily rainfall data from the weather stations.

4) Ancillary Data: The combined Aqua + Terra Moderate Resolution Imaging Spectroradiometer (MODIS) land cover product (MCD12Q1 version 6) provides annual land cover maps with a spatial resolution of 500 m [55]. Among the five different land cover classifications, this study used the MODIS International Geosphere-Biosphere Program-Land Cover (IGBP-LC). This classification contains 17 classes based on three canopy components: above ground biomass (perennial and annual), leaf longevity (evergreen and deciduous), and leaf type (needleleaf, broadleaf, and grasses). These are critical variables for seasonal climate and carbon-balance modeling, carbon cycle and land energy transfer, and for explaining gas exchange characteristics [56]. For the purpose of this research, the IGBP-LC map was aggregated from the original 500 m to 25 km using the most frequent class, and the 17 classes proposed by the IGBP were aggregated into the four main land cover types (savannas, croplands, grasslands, and shrublands) within the study area. Fig. 1 shows the resulting land cover map over the Iberian Peninsula.

Data from morning passes of the SMAP Enhanced L2 Radiometer Half-Orbit 9-km EASE-Grid Soil Moisture, Version 4 (SPL2SMP_E) and SPL2SMAP_S products were used in this study. The SPL2SMP_E product is the result of extracting the maximum information from the SMAP antenna by taking advantage of the SMAP radiometer oversampling to generate an enhanced radiometer-based SM product, posted in a 9-km EASEv2 grid. SPL2SMAP_S product is already explained in Section II-B2. These two products contain the ancillary data used to estimate the SM—e.g., ω, h_s, τ, T_s, and vegetation water content (VWC). Here, we use τ (at nadir) and T_S provided in a 1- and 9-km EASEv2 grid and VWC in a 1-km EASEv2 grid.

A map of clay fraction (CF) was also required. It is provided by the National Snow and Ice Data Center (NSIDC) in a 9-km

EASEv2 grid within the SMAP L1-L3 Ancillary Static Data, Version 1[57].

III. Methodology

This section is devoted to detail the data preprocessing and methodological approach followed in this study.

A. Data Preprocessing and Methodology Overview

The flowchart in Fig. 2 shows the three analyses carried out in this study: 1) calibration of the ω and h_s parameters; 2) downscaling of the SMOS TB_V to 1 km; and 3) retrieval of high-resolution SMOS SM. The flowchart includes the input parameters used in each step and the grid pixel size to which all input data are expressed in order to operate with them. In the ω and h_s calibration step, all data are aggregated to a 25-km EASEv2 grid (see "Aggregation to LR" block in Fig. 2), while for the other two steps, the data are resampled to a 1-km EASEv2 grid (see "Resampling to HR" block in Fig. 2). The aggregation is done by averaging the values of all the samples contained within each pixel of the target grid. For the resampling to 1 km, nearest neighbor interpolation is used.

The next sections detail the methodology of each processing block shown in Fig. 2.

B. Calibration of ω and h_s

Over the last years, a variety of SM retrieval approaches using L-band radiometry have been proposed (see Section I for details). Among these, those that use both horizontal and vertical polarizations (e.g., DCA, MT-DCA, LPRM, or SMOS-IC) can simultaneously retrieve SM and another parameter, usually τ. Furthermore, these techniques can benefit from the high sensitivity to SM due to the high contrast between TB_H and TB_V at higher incidence angles [14], [58]. In a previous study, we tested the LPRM algorithm to calibrate ω and h_s parameters over the Iberian Peninsula for 2016. We obtained a very good performance when comparing the resulting SM maps against the SM observations from the REMEDHUS network, with correlations (R) always higher than 0.81, a bias lower than 0.015 m^3/m^3, and an unbiased root mean square error (ubRMSE) of about 0.04 m^3/m^3 (SMOS target accuracy) [59]. Since Sentinel-1 only measures VV + VH polarizations over land, only disaggregated SMOS TB at vertical polarization can be obtained with the approach in [22], as will be detailed in Section III-C. For this reason, we opted for SCA_V, which only needs TB at vertical polarization to estimate SM from both coarse (SMOS) and fine scale (SMOS/Sentinel-1).

The SCA is a reliable technique [60], straightforward to implement and computationally fast enough for the purpose of this study. It allows to retrieve SM using the effective soil temperature (T_s), the TB at one polarization, and the optimal ω [61] and h_s values. The SCA is based on the $\tau\omega-$ model [13]

$$\begin{aligned} TB_p = {} & e_{r,p} T_s \gamma + (1-\omega) T_c (1-\gamma) \\ & + (1-e_{r,p})(1-\omega)(1-\gamma) T_c \gamma \end{aligned} \quad (1)$$

where the subscript p refers to the polarization (vertical in our case), $\gamma = e^{-\tau/\cos\theta}$ is the transmissivity, τ corresponds to the vegetation optical depth, θ is the SMOS incidence angle (32.5°, 42.5°, or 52.5°), ω denotes the single scattering albedo, and T_c stands for the canopy temperature. Thermal equilibrium is assumed ($T_s \approx T_c$) in the SCA, an approximation already used in other microwave-based retrieval algorithms [15], [16], [22]. The emissivity of a rough surface (e_r) is calculated as follows:

$$e_{r,p(1)} = 1 - \left((1-Q)R_{s,p(1)} + QR_{s,p(2)}\right)e^{-h_s \cos^{N_{r,p}}(\theta)} \quad (2)$$

where the subscripts $p(1)$ and $p(2)$ are the two polarizations (vertical and horizontal), Q is the polarization mixing factor, $R_{s,p}$ is the smooth surface reflectivity calculated using the Fresnel equations, and $N_{r,p}$ represents the change in the angular dependence of the reflectivity due to the soil roughness. The polarization mixing factor is assumed very small for L-band, and here, it has been set to $Q = 0$ to simplify the model [14], [60], [62], [63]. The Fresnel equations require the dielectric constant that is estimated with the Mironov mixing model [64] and $N_{r,p}$ is set to 2 [60].

1) Multiangular Parametrization: The following steps were conducted to obtain the optimized ω and h_s values.

1) Sensitive ranges were considered for the parameters, with ω varying between 0 and 0.22 (in steps of 0.02) and h_s between 0 and 0.2 (in steps of 0.01). Daily SM was retrieved using the SCA_V for each pair of ω and h_s values and for each low-resolution pixel within the study area. In this step, the BEC SMOS L3 TB was used at a 25-km grid, rather than a 12.5-km grid, due to the large number of SM estimates required.
2) The resulting SM time series obtained for each pixel of the study area was compared with the SM used as reference. Four statistical metrics were considered [65]: R, ubRMSE, bias, and STD. These statistics were averaged by land-cover type (savannas, croplands, grasslands, and shrublands), and for each pair of ω and h_s, the optimal ω and h_s values are those that provide the best match, on average, of the resulting SM estimates compared to the reference SM.

The procedure described above was carried out independently for the three proposed incidence angles. At the 42.5° incidence angle, ERA5-land SM was used as reference due to its independence from SM estimates from remote sensing sensors. Observations are not directly used in the production of ERA5-land, but they may have an indirect influence through the atmospheric forcing used. Since a positive bias of ERA-land SM (ERA5-land SM minus *in situ*) was reported [52], the optimization of ω and h_s at 42.5° was carried out using R and ubRMSE exclusively. Furthermore, the optimal ω and h_s values were selected by comparing them with the results obtained in previous studies that also use the SCA_V to retrieve SM at a similar incidence angle [60].

Since there is no specifically calibrated values of SCA_V reported in literature for 32.5° and 52.5° angles, the procedure discussed above could not be followed for these two angles. Then, the optimal ω and h_s values for these two angles were selected using as reference the SM obtained through the SCA_V for the 42.5° incidence angle. The R, ubRMSE, bias, and difference of STD were used as optimization criteria.

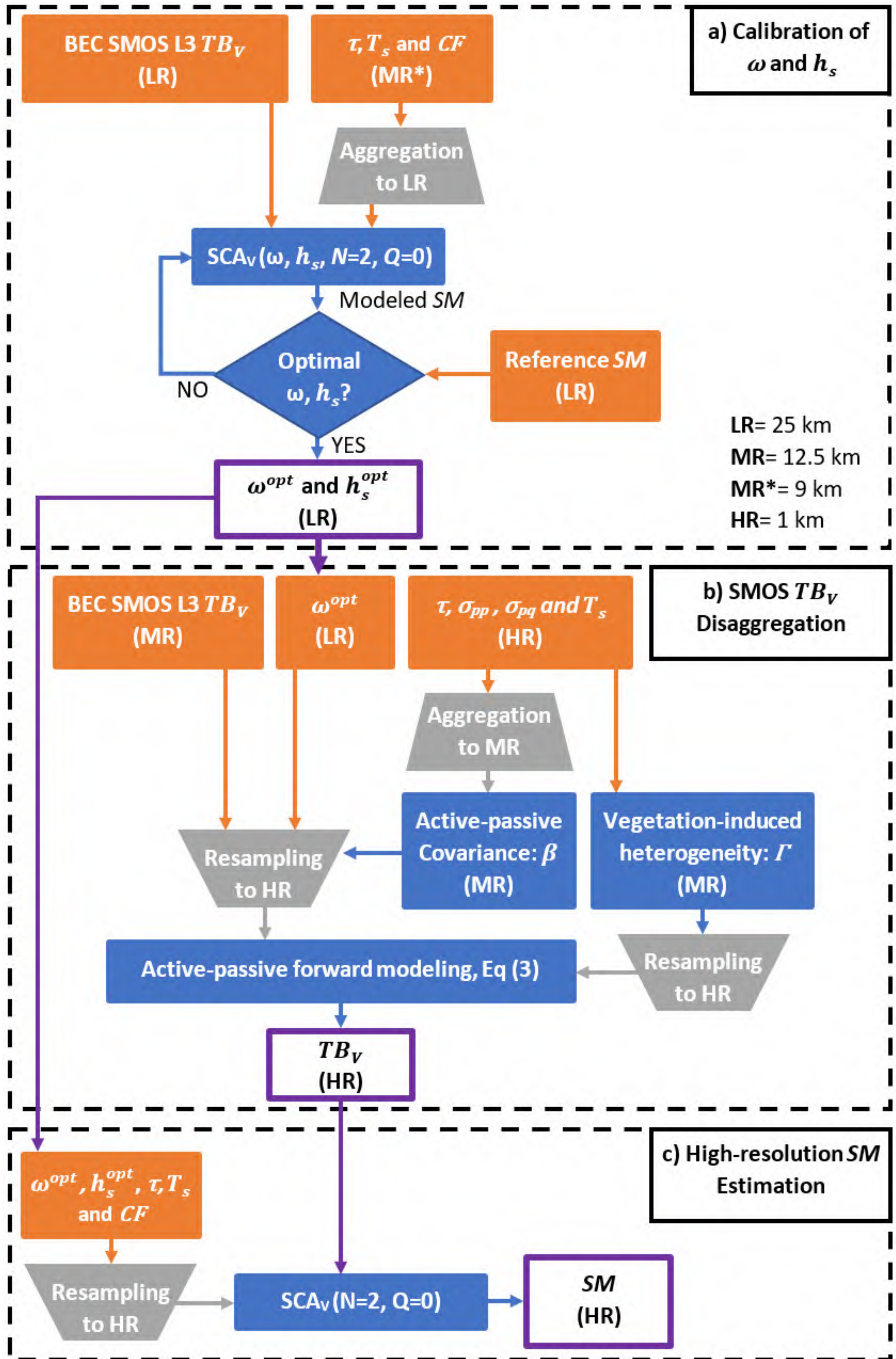

Fig. 2. Methodology flowchart. (a) Calibration of ω and h_s, (b) disaggregation of the SMOS TB$_v$, and (c) retrieval of the SMOS high-resolution SM maps. The orange boxes are the required input parameters for each of the three main analyses. The blue boxes are the different operations applied to the input data. The purple boxes are the results obtained at the end of each of the three main processing blocks (dashed black blocks).

2) Low-Resolution SM and Validation of Retrieval Model Parametrization: Daily SM maps were obtained through the application of the SCA$_V$ algorithm with the optimal ω and h_s values to the SMOS TB$_V$ at 25 km. Time series of the three

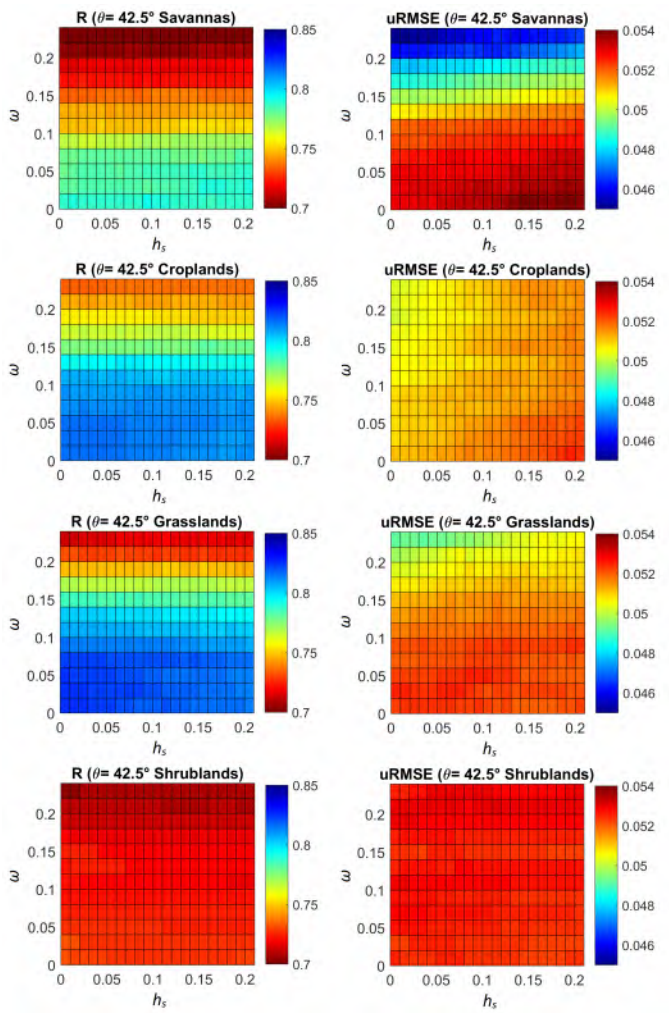

(a) (b)

Fig. 3. Mean (a) R and (b) ubRMSE between retrieved SCA_V SM at 42.5° incidence angle and ERA5-land SM for each possible ω and h_s value and for each land cover (savannas, croplands, grasslands, and shrublands) using all pixels over the Iberian Peninsula.

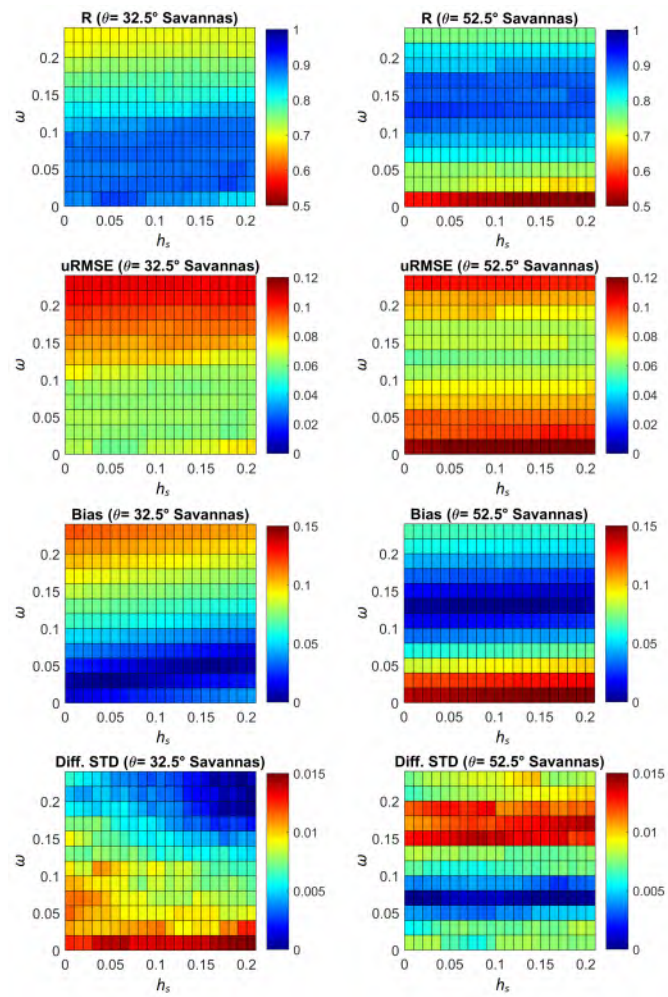

(a) (b)

Fig. 4. Mean R, ubRMSE, bias, and difference of STD between retrieved SCA_V SM at 42.5° and retrieved SCA_V SM at (a) 32.5° and (b) 52.5° for each ω and h_s value in savanna.

SM data streams (32.5°, 42.5°, and 52.5°) over REMEDHUS was obtained and compared against the SM from *in situ* stations. Among all the stations available within the REMEDHUS network, seven were selected (F11, H13, J12, J14, K10, M9, and O7). They are located in a rainfed/fallow land use, which is the most representative land use at the SMOS spatial scales, at low (25 km) and high resolution (1 km) [66]. Hourly recorded measurements of these stations were aggregated to a daily [67] and spatially average within the satellite pixel, before using them as a benchmark to validate the different products.

C. *SMOS* TB_V *Disaggregation*

The active–passive downscaling algorithm [22] proposed by the Jet Propulsion Laboratory (JPL) was originally developed to disaggregate the SMAP TB_V maps. In this study, the SMAP TB_V has been replaced by the BEC SMOS L3 TB_V to adapt the algorithm as follows:

$$\text{TB}_{p,\theta}(\text{HR}) = \Bigg[\frac{\text{TB}_{p,\theta}(\text{MR})}{T_s} + \beta(\text{MR}) \cdot \Big\{\big[\sigma_{pp}(\text{HR}) - \sigma_{pp}(\text{MR})\big] + \Gamma(\text{MR}) \cdot \big[\sigma_{pq}(\text{MR}) - \sigma_{pq}(\text{HR})\big]\Big\}\Bigg] \cdot T_s \tag{3}$$

where MR accounts for medium resolution (12.5 km) and HR for high resolution (1 km), $\text{TB}_{p,\theta}(\text{HR})$ is the disaggregated SMOS brightness temperature at 1 km, $\text{TB}_{p,\theta}(\text{MR})$ corresponds to the satellite observed single-angle SMOS brightness temperature at 12.5 km, $\sigma_{pp}(\text{MR})$ and $\sigma_{pq}(\text{MR})$ denote the Sentinel-1 co- and cross-polarization backscatter aggregated to 12.5 km, $\sigma_{pp}(\text{HR})$ and $\sigma_{pq}(\text{HR})$ are the Sentinel-1 co- and cross-polar backscatter aggregated to 1 km, and $\Gamma(\text{MR})$ and $\beta(\text{MR})$ are defined in the active–passive downscaling algorithm [22]. The Γ parameter represents the vegetation-induced heterogeneity within the MR radiometer pixel that is detected by the high-resolution $\sigma_{pp}(\text{HR})$ and $\sigma_{pp}(\text{HR})$ radar observations [41]. Γ is estimated as the slope of the linear regression between the high-resolution $\sigma_{pp}(\text{HR})$ and $\sigma_{pq}(\text{HR})$

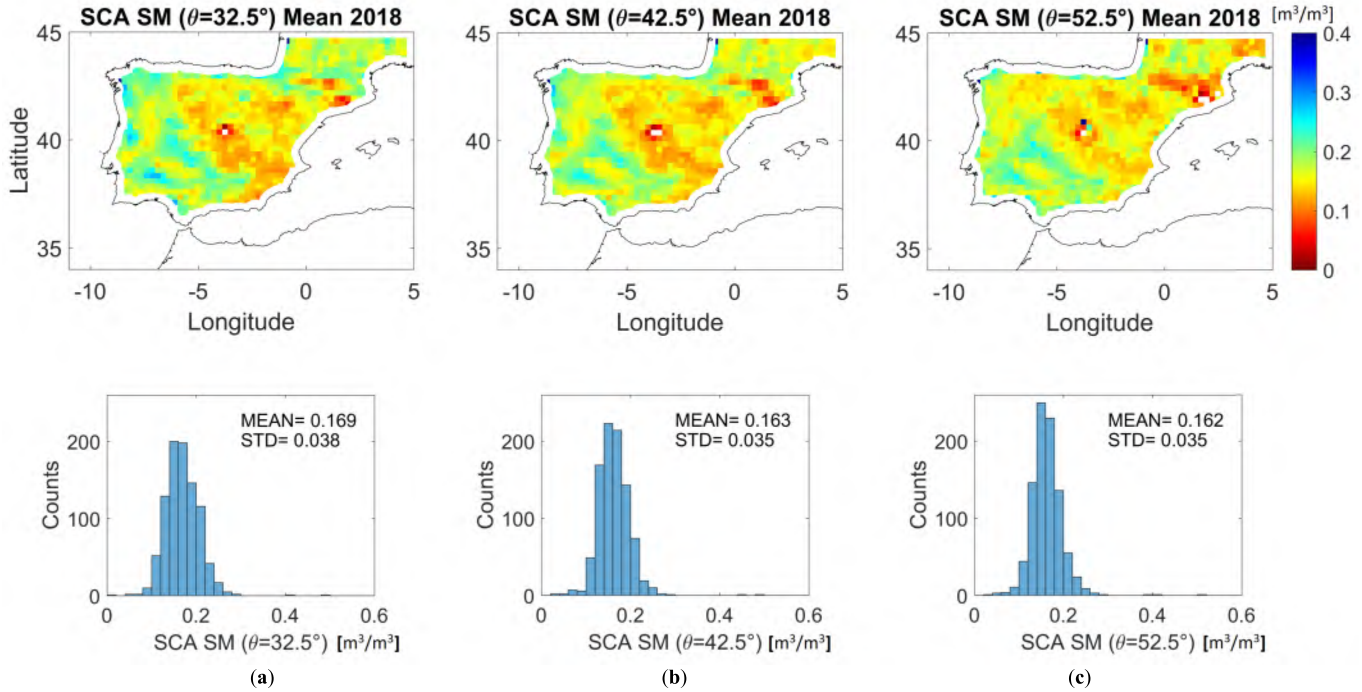

Fig. 5. Maps of SCA$_\mathrm{V}$ SM averaged over time (2018) obtained at (a) 32.5°, (b) 42.5°, and (c) 52.5° using the optimal values of ω and h_s presented in Tables II and III and their respective histograms.

values contained within the domain of an MR pixel [41], [68]

$$\Gamma(\mathrm{MR}) = \left[\frac{\partial\sigma_{pp}(\mathrm{HR})}{\partial\sigma_{pq}(\mathrm{HR})}\right]_{\mathrm{MR}}. \tag{4}$$

The $\beta(\mathrm{MR})$ parameter represents the covariation between SMOS TB$_V$ and the Sentinel-1 backscatter (VV–VH)

$$\beta(\mathrm{MR}) = \frac{\frac{\mathrm{TB}_{p,\theta}(\mathrm{MR})}{T_s} - (\gamma + (1-\omega)(1-\gamma))}{\sigma_{pp}(\mathrm{MR}) - \Gamma \cdot \sigma_{pq}(\mathrm{MR})}. \tag{5}$$

It represents the change in emission for a unit change in backscatter. This study uses the snapshot approach, where β values are calculated for each overpass without requiring time series. The variables involved in the computation of β are: ω, τ, T_s, σ, and TB$_{p,\theta}$. Optimal ω values at 25 km were obtained through the SCA$_\mathrm{V}$ retrieval algorithm for each incidence angle and for each land cover, as explained in Section III-B1. The use of TB$_{p,\theta}$(MR) at MR instead of at low resolution is chosen to minimize the boxing effect (the outline of the low-resolution pixels visible in the high-resolution maps) in the resulting disaggregated TB$_V$ (3). The rest of these variables (T_S, τ, and σ) were provided within the SMAP product SPL2SMAP_S on a 1-km grid. In order to have all the inputs in the same grid and to enable easy data handling, they were resampled into a 12.5-km EASEv2 grid. β was calculated with the ancillary data described here and its behavior was analyzed for the three SMOS incidence angles considered (32.5°, 42.5°, and 52.5°), the Sentinel-1 incidence angles, and the VWC. Finally, (3) was applied to obtain three SMOS TB$_V$ datasets with a spatial resolution of 1 km, one for each incidence angle.

D. High-Resolution SM Estimation

To retrieve the SM at 1 km, from the disaggregated SMOS TB$_V$ (see Section III-C), the SCA$_\mathrm{V}$ model was applied. The required variables are: T_s, τ, CF, h_s, ω, and TB$_{p,\theta}$(HR). T_s and τ are provided within the SMAP product SPL2SMAP_S in a 1-km grid. CF is provided by the NSIDC in a 9-km grid. h_s and ω are obtained through the SCA$_\mathrm{V}$ algorithm, as explained in Section III-B1, in a 25-km EASEv2 grid. TB$_{p,\theta}$(HR) is already at 1 km. In order to have all the inputs in the same grid, they have been resampled into a 1-km EASEv2 grid.

IV. Results and Discussion

This section is devoted to: 1) showing the optimal values of ω and h_s at three SMOS incidence angles (32.5°, 42.5°, and 52.5°) for four land covers (savannas, croplands, grasslands, and shrublands) and validating these parameters through the retrieved SM [see Fig. 2(a)]; 2) analyzing both the resulting active–passive covariation (β) values and the disaggregated SMOS TB$_V$ maps at the three analyzed incidence angles [see Fig. 2(b)]; and 3) showing the first high-resolution SM maps at each incidence angle obtained from the disaggregated SMOS TB$_V$ [see Fig. 2(c)].

A. Performance of Single Channel Algorithm Applied to SMOS TB

1) Calibration of Multiangular Model Parametrization: Fig. 3 shows the mean R and ubRMSE obtained through the comparison of the estimated SCA$_\mathrm{V}$ SM at the 42.5° incidence angle and ERA5-land SM, which is used as reference to calibrate ω and h_s parameters. Results are obtained independently for savannas, croplands, grasslands, and shrublands.

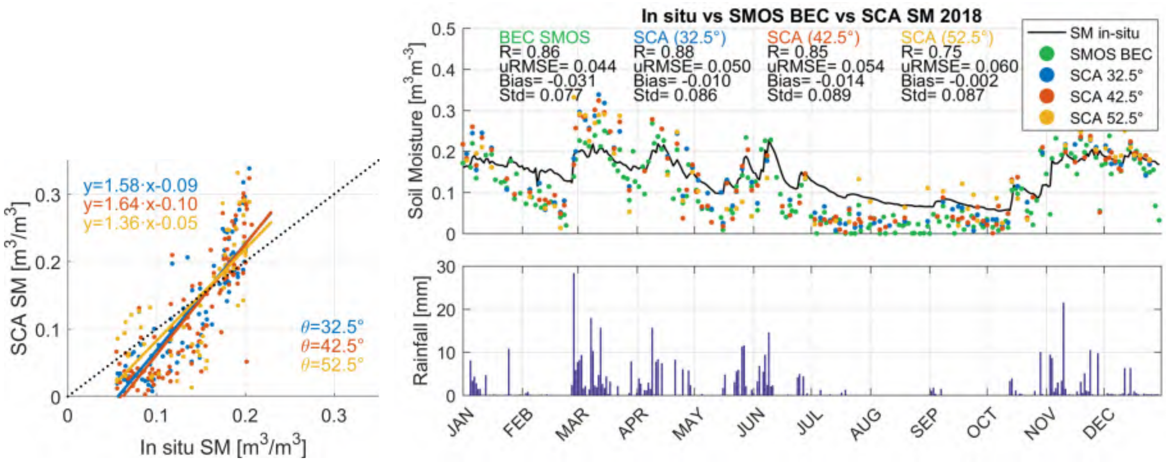

(a) (b)

Fig. 6. (a) Retrieved SCA_V SM at 32.5° (blue), 42.5° (red), and 52.5° (yellow) versus *in situ* SM from REMEDHUS. (b) Daily evolution of *in situ* SM from REMEDHUS (Top; black), BEC SMOS L3 SM (Top, green), the three retrieved SCA_V SM at 32.5°, 42.5°, and 52.5°, and daily rainfall (Bottom).

TABLE II

OPTIMAL ω AND h_s VALUES AND MEAN R AND UBRMSE BETWEEN RETRIEVED SCA_V *SM* AT 42.5° INCIDENCE ANGLE AND ERA5-LAND *SM* OBTAINED FOR FOUR LAND COVERS (SAVANNAS, CROPLANDS, GRASSLANDS, AND SHRUBLANDS), USING ALL PIXELS OVER THE IBERIAN PENINSULA. THE SMAP SCA ω AND h_s VALUES HAVE ALSO BEEN INCLUDED

	$\Theta = 42.5°$					
	ω	ω (SMAP)	h_s	h_s (SMAP)	R	ubRMSE [m^3/m^3]
Savannas	0.06	0.08	0.09	0.156	0.78	0.053
Croplands	0.06	0.05	0.08	0.108	0.81	0.051
Grasslands	0.06	0.05	0.15	0.156	0.82	0.052
Shrublands	0.04	0.05	0.10	0.11	0.73	0.053

As a general trend, it can be seen that R decreases as ω increases in all land covers. For savannas and grasslands, the ubRMSE decreases as ω increases, while for croplands and shrublands, it remains almost constant for the entire range of values. On the other hand, the effect of h_s on the results is minimal, both in R and ubRMSE. Final calibration of ω and h_s at 42.5° was done according to previous studies in literature, by comparing our obtained results (see Fig. 3) with those obtained with the same SM retrieval algorithm at a similar incidence angle [60]. Table II shows the selected optimal values of ω and h_s at 42.5° for each land cover and their respective performance metrics. The optimal value of ω is set to 0.6 for all the land covers, except for shrublands, which have a slightly lower value of 0.4. The optimal h_s fluctuates between 0.08 and 0.15. The highest mean correlation (R) is obtained for grasslands and croplands (0.82 and 0.81, respectively) and the lowest one is received for shrublands (0.73). The mean ubRMSE is about 0.05 m^3/m^3 considering the four land covers.

In order to find the optimal ω and h_s values at the other two analyzed SMOS incidence angles (32.5° and 52.5°), four statistics (R, ubRMSE, bias, and difference of STD) are computed between the retrieved SCA_V SM at 42.5° and the retrieved SCA_V SM at 32.5° and 52.5°, independently for each land cover type. Fig. 4 shows the performance metrics in the savanna land cover, for the 32.5° [see Fig. 4(a)] and 52.5° [see Fig. 4(b)] incidence angles. At 32.5°, R decreases while the ubRMSE and the bias increase as ω increases. Again, the effect of h_s on the results is low, with slightly better statistical performance for higher values. At 52.5°, the optimal ω values are shifted to higher values, while optimal h_s is shifted to lower values. Note that even the highest values of STD differences (~0.015 m^3/m^3) are low enough to neglect this statistic when choosing $\omega$and h_s values. Similar behaviors were displayed for the other land covers (not shown). The optimal ω and h_s values at 32.5° and 52.5°, together with their respective statistics, are summarized in Table III. The optimal values of ω range between 0.02 and 0.04, while h_s is comprised between 0.12 and 0.18, at 32.5°. At 52.5°, the optimal albedo value is set to 0.12 for all four land cover regions, and h_s ranges from 0.01 to 0.05. Both at 32.5° and 52.5°, the mean R is always equal or higher than 0.9. The mean bias reaches a peak of 0.016 m^3/m^3 at 52.5° for shrublands. Analyzing Tables II and III, an ascending trend is revealed for ω and a descending trend is found for h_s, as the SMOS incidence angle increases.

The retrieval algorithm used in this research (SCA_V) was the original postlaunch baseline algorithm for the SMAP mission from 2015 to 2021. In the SMAP algorithm [60], h_s values are slightly higher (0.156, 0.108, 0.156, and 0.11 for savannas, croplands, grasslands, and shrublands, respectively) than those proposed in this study (see Table II). As it was already analyzed by Wigneron *et al.* [69], these h_s values used in SMAP have a narrower range compared to those used in the SMOS baseline algorithm [70], where h_s varies between 0.1 and 0.3. In other global studies, h_s is considered constant, as in [9], where the MT-DCA was applied to Aquarius data to retrieve SM, τ, and ω at L-band by assuming a constant h_s of 0.13 in time and space. Regarding ω, the SMAP algorithm uses a value of 0.05 for croplands, grasslands, and shrublands, in line with those proposed in Table II, and a slightly higher value of 0.08 for savannas. Moreover, a global scale study conducted by

TABLE III

OPTIMAL ω AND h_s VALUES AND MEAN R, UBRMSE, BIAS, AND STD DIFFERENCE BETWEEN RETRIEVED SCA$_V$ SM AT 32.5°/52.5° INCIDENCE ANGLES AND RETRIEVED SCA$_V$ SM AT 42.5°, OBTAINED FOR FOUR LAND COVERS (SAVANNAS, CROPLANDS, GRASSLANDS, AND SHRUBLANDS)

	$\Theta = 32.5°$						$\Theta = 52.5°$					
	ω	h_s	R	ubRMSE [m^3/m^3]	Bias [m^3/m^3]	Diff. STD. [m^3/m^3]	ω	h_s	R	ubRMSE [m^3/m^3]	Bias [m^3/m^3]	Diff. STD. [m^3/m^3]
Savannas	0.04	0.18	0.9	0.058	0.004	0.009	0.12	0.03	0.92	0.056	0.003	0.008
Croplands	0.04	0.12	0.98	0.019	0.003	0.006	0.12	0.05	0.98	0.021	0.008	0.004
Grassland	0.04	0.16	0.98	0.020	0.000	0.005	0.12	0.02	0.94	0.041	0.005	0.005
Shrubland	0.02	0.15	0.99	0.010	0.005	0.002	0.12	0.01	0.98	0.019	0.016	0.002

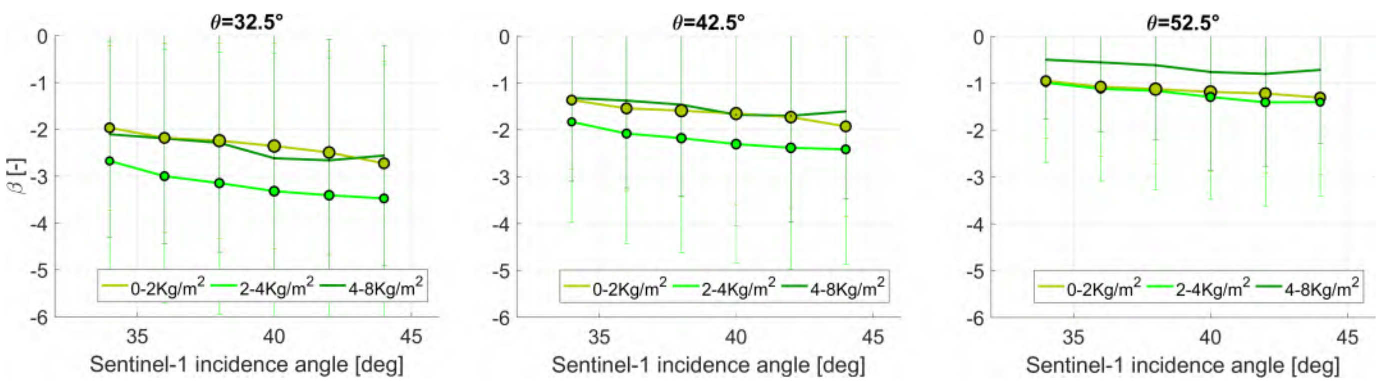

(a) (b) (c)

Fig. 7. Active–passive microwave covariation parameter β along Sentinel-1 incidence angle for three VWC ranges, obtained independently at (a) 32.5°, (b) 42.5°, and (c) 52.5° SMOS incidence angles. The position of the circles represents the mean values, and its size the number of samples (the larger the circle, the higher the number of samples, and vice versa). Note that due to the few densely vegetated areas available in the Iberian Peninsula, the number of β samples for the highest VWC class (4–8 kg/m^2) is very low.

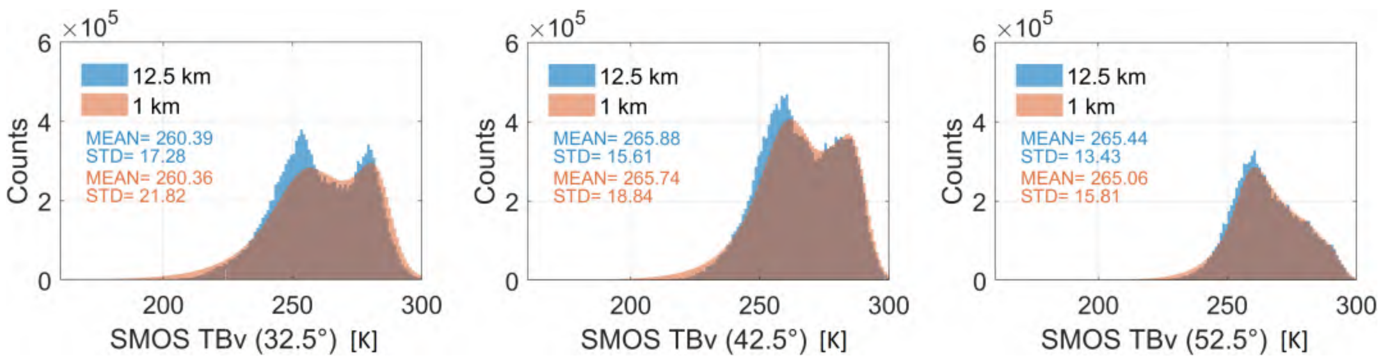

(a) (b) (c)

Fig. 8. SMOS TB$_V$ histograms of data over the Iberian Peninsula for the year 2018, obtained independently at (a) 32.5°, (b) 42.5°, and (c) 52.5°. In blue, the initial SMOS TB$_V$ at 12.5 km, and in red, the disaggregated SMOS TB$_V$ at 1 km.

Van der Schalie *et al.* [15] applied the LPRM to SMOS observations for optimizing ω. An optimal ω of 0.12 was found, invariant in space and time, and independent of the tested incidence angles (from 42.5° to 57.5°). From Tables II and III, it can be seen that the retrieved ω values of this study are almost invariant with the IGBP-LC classes. This low sensitivity was also detected by Fernandez-Moran *et al.* [16], where a global optimal value of $\omega = 0.10$ was selected to estimate SM and τ from SMOS multiangular data (from 20° to 55°), and by Karthikeyan *et al.* [18] where a global fixed value of $\omega = 0.06$ was assumed to estimate SM, τ, and h_s from X-band AMSR-E observations.

2) Validation of Retrieved Low-Resolution SM: Fig. 5 shows the temporal average of the retrieved daily SM maps and their respective histograms, for the year 2018, at each incidence angle. These results were obtained by applying the SCA$_V$ to SMOS TB$_V$ at 25 km with the optimal ω and h_s parameterizations (see Tables II and III). These maps show similar spatial patterns, mean, and STD. The mean ranges from 0.162 to 0.169 m^3/m^3 and the STD from 0.035 to 0.038 m^3/m^3.

Fig. 6(a) displays the agreement between the single-angle SCA$_V$ SM at 32.5°, 42.5°, and 52.5° and REMEDHUS *in situ* time series. SCA$_V$ SM shows a slope close to the 1:1 line

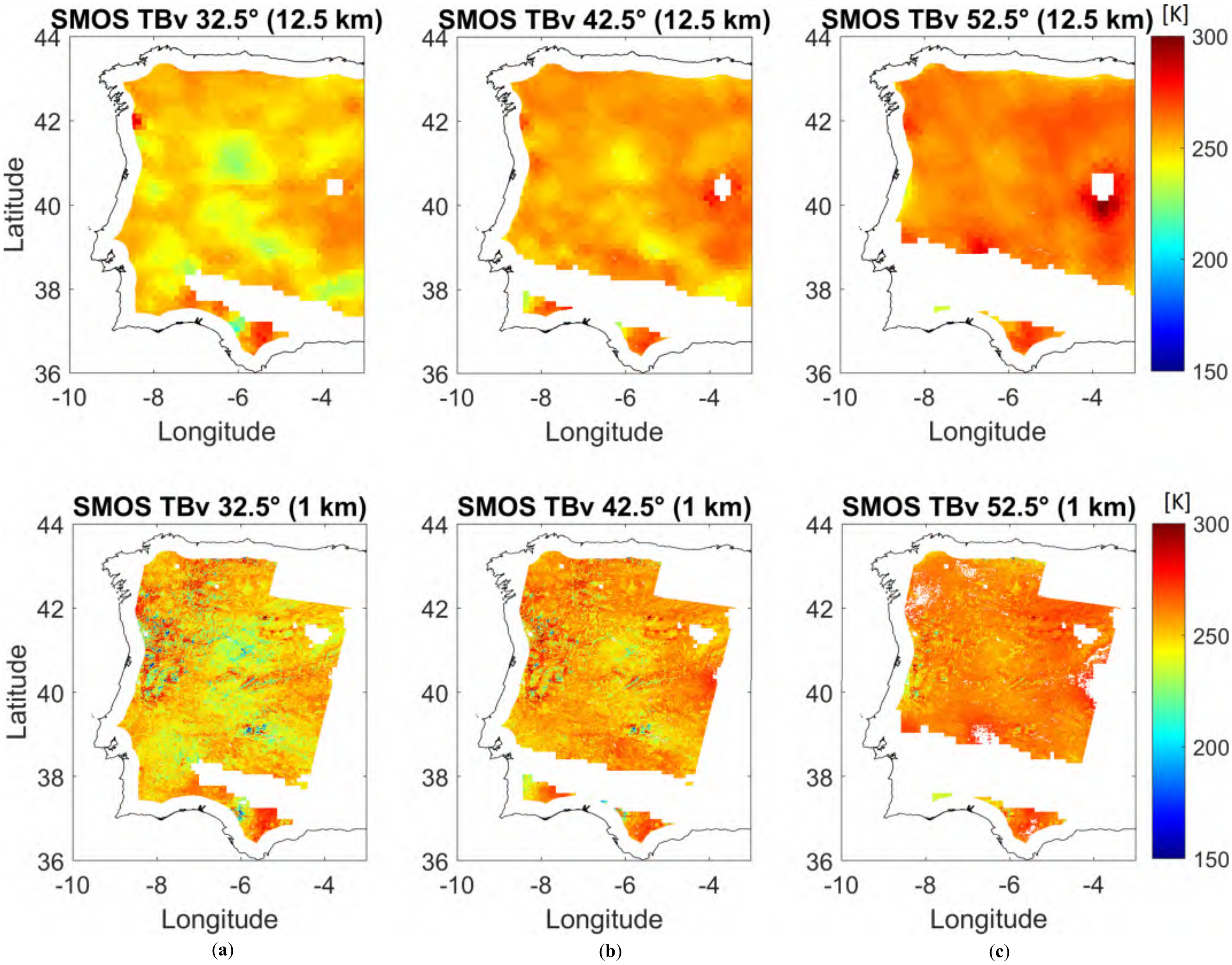

Fig. 9. SMOS TB_V maps for January 3, 2018, obtained independently at (a) 32.5°, (b) 42.5°, and (c) 52.5°. At the top, the initial SMOS TB_V in a grid of 12.5 km, and at the bottom, the disaggregated SMOS TB_V at 1 km.

but also a clear dry bias with respect to *in situ* SM. This effect can also be seen in Fig. 6(b) (top), where the time series of multiangular BEC SMOS L3 SM and single-angle retrieved SCA_V SM at 32.5°, 42.5°, and 52.5° are plotted and statistically compared with the *in situ* measurements using the *R*, ubRMSE, bias, and the STD metrics, also added to this figure. Course of daily precipitation acquired over REMEDHUS is also shown (bottom). All SCA_V SM, retrieved at the three incidence angles independently, agree reasonably well between each other and show similar temporal patterns when compared against the BEC SMOS L3 SM product. They are able to capture wet up and dry down events. Regarding the performance of the SM retrieval at the three different incidence angles, *R* oscillates between 0.75 (at 52.5°) and 0.88 (at 32.5°). The ubRMSE slightly increases with the increase of the incidence angle, ranging from 0.05 to 0.06 m^3/m^3. The three of them have a negative bias with respect to *in situ* SM. This bias remains almost constant along time, but it can turn positive after heavy rain events, as in March 2018. Underestimation of the SMOS SM with respect to *in situ* measurements has already been highlighted in previous studies [21], [36], [66], [71], the so-called "dry bias." As reported in [72], this "dry bias" could

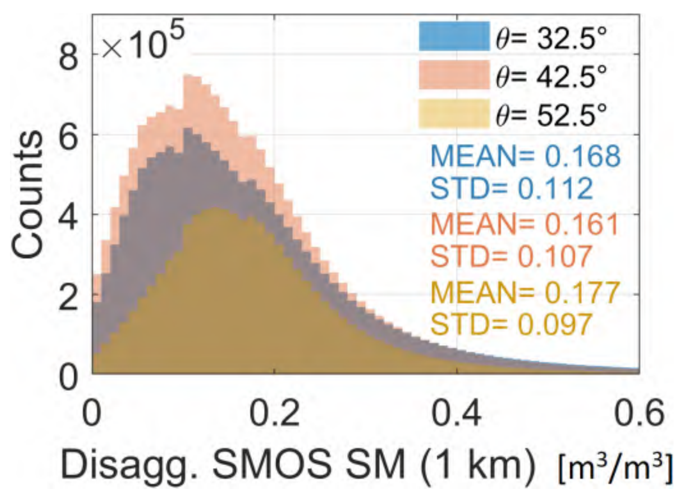

Fig. 10. Histograms of the high-resolution SCA_V SM at 32.5° (blue), 42.5° (red), and 52.5° (yellow).

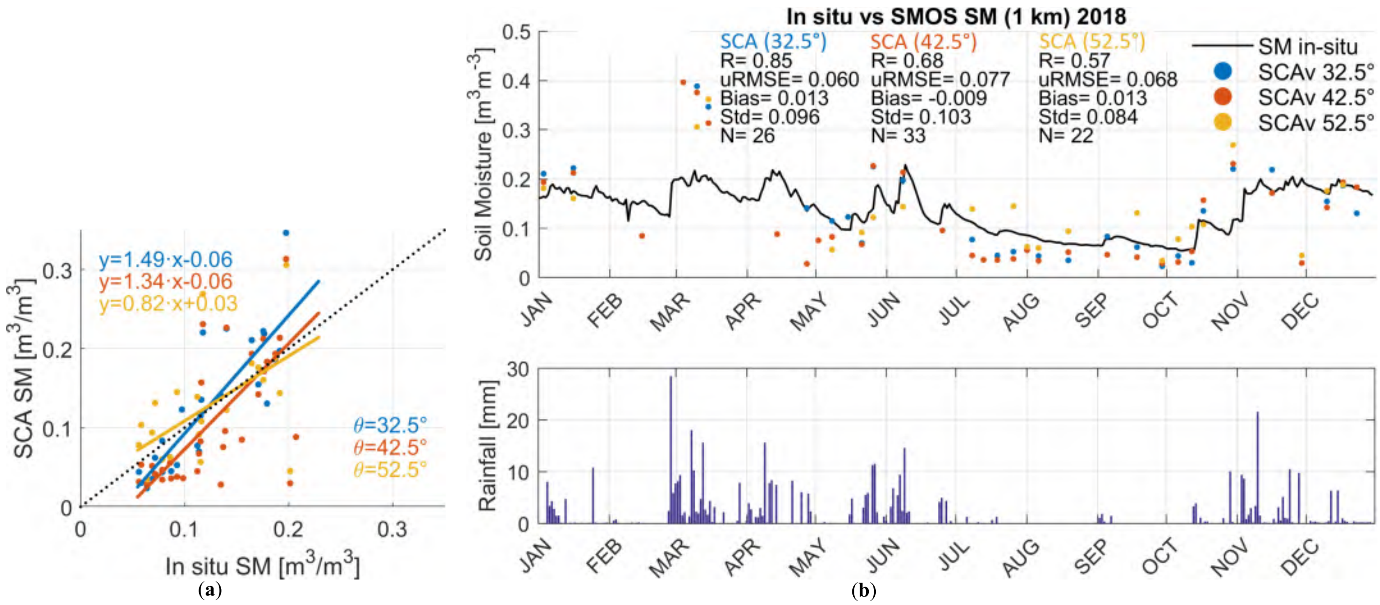

Fig. 11. (a) Retrieved high-resolution SCA_V SM at 32.5° (blue), 42.5° (red), and 52.5° (yellow) versus *in situ* SM from REMEDHUS. (b) Daily evolution of *in situ* SM from REMEDHUS (Top; black), the three retrieved high-resolution SCA_V SM at 32.5°, 42.5°, and 52.5°, and daily rainfall (Bottom).

be the result of underestimating the effective soil temperature. In this study, the applied soil temperature is derived from the National Aeronautics and Space Administration (NASA) Goddard Earth Observing System (GEOS)-5 models. A possible underestimation of the soil temperature would lead to an overestimation of the soil microwave emissivity, resulting in an underestimation of SM. Moreover, there is an inherent scale gap when comparing a point-scale *in situ* measurement at REMEDHUS against an area-averaged satellite-based SM estimation, which could also explain this mismatch between *in situ* and satellite observations.

B. Analysis of Active–Passive Covariation and Disaggregated SMOS TB

Fig. 7 shows the active–passive microwave covariation β between SMOS and Sentinel-1 for different Sentinel-1 incidence angle bins (from 34° to 44°) and for three VWC ranges (0–2, 2–4, and 4–8 kg/m^2). The analysis is independently performed for 32.5°, 42.5°, and 52.5° SMOS incidence angles. It can be observed that β values gradually and gently decrease with increasing Sentinel-1 incidence angle. This effect was also found in a previous study conducted by Jagdhuber *et al.* [41], where the active–passive covariation between SMAP ($\theta = 40°$) and Sentinel-1 was analyzed. Jagdhuber *et al.* suggested that the dependence of the active–passive covariation on the Sentinel-1 incidence angle was increasingly masked by denser vegetation. We not only provided β behavior as a function of the Sentinel-1 angle but also in relation to different SMOS angles. The largest variation (sensitivity), in magnitude of β, is around d 0.7 at the 32.5° SMOS angle [see Fig. 7(a)]. β dependence with Sentinel-1 angle is less evident for higher SMOS angles, being almost insensitive to Sentinel-1 angle variations. A clear trend of β with the SMOS incidence angle is also observed; the larger the SMOS angle, the closer the values are to zero, which translates into a loss of backscatter sensitivity to changes in emissivity, for the highest SMOS incidence angle (52.5°).

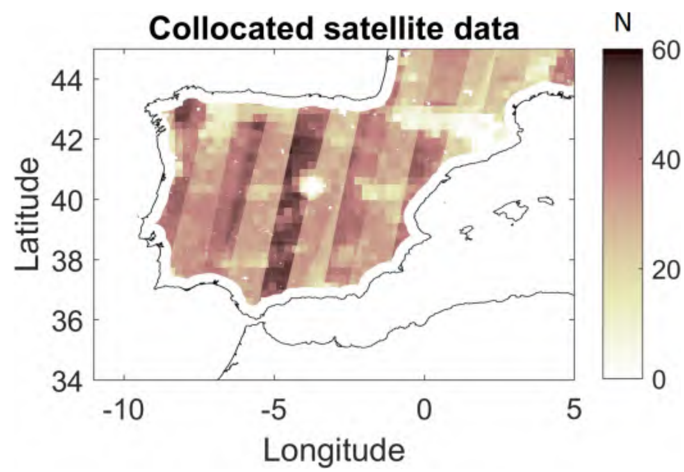

Fig. 12. Number of concurrent samples of SMOS, SMAP, and Sentinel-1 for the year 2018.

The histograms of the initial SMOS TB_V in a 12.5-km grid and the disaggregated SMOS TB_V at 1 km, obtained from (3), are displayed in Fig. 8. They are obtained using the information of the entire study region along the year 2018. The spread of the distribution is similar for both products with slightly higher differences at 32.5°. The mean difference never exceeds 0.38 K for any of the three SMOS incidence angles, with an STD that is always higher for the disaggregated estimations. Differences between high and low resolution can be partially explained by the fact that the Sentinel-1 signal at C-band, used to disaggregate the SMOS TB_V, cannot penetrate through dense or tall vegetation [41], [73]. Fig. 8 shows that the number of samples is lower for 32.5° and 52.5°

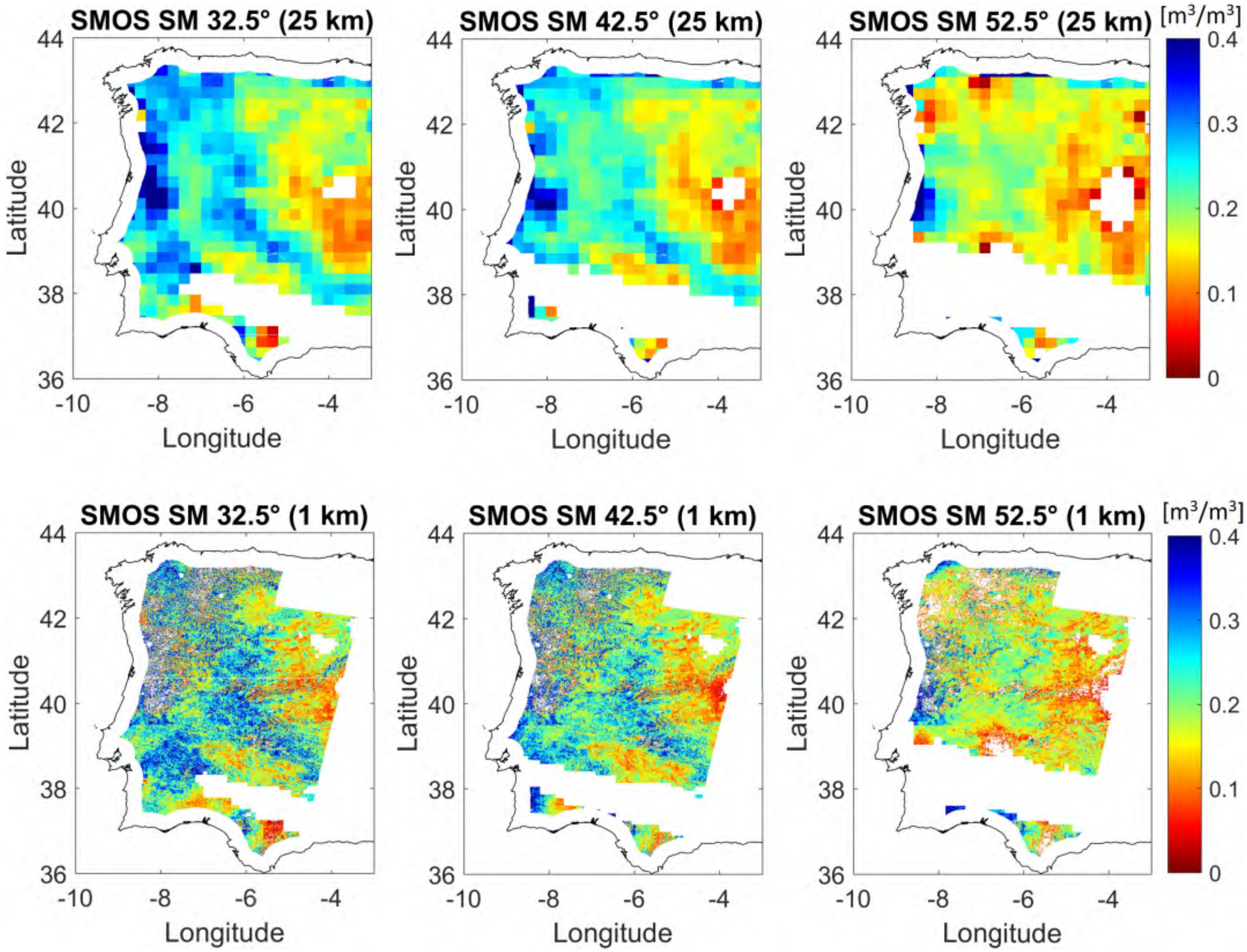

(a) (b) (c)

Fig. 13. Retrieved SMOS SM maps for January 3, 2018, at 25 km (Top) and 1 km (Bottom), obtained independently at (a) 32.5°, (b) 42.5°, and (c) 52.5° incidence angles using the parameters presented in Tables II and III.

compared to 42.5°. This could be explained by the shape of the alias-free field of view of the SMOS instrument, from which the incidence angles, sorted from highest to lowest spatial coverage, are 42.5°, 32.5°, and 52.5° [74].

The SMOS TB_V maps at low and high resolution for 32.5°, 42.5°, and 52.5° are presented in Fig. 9 for January 3, 2018. Similarities in the spatial patterns can be easily detected, in agreement with the results of Fig. 8. From Fig. 9, it can also be understood that the TB_V maps, both at high and low resolution, are highly affected by RFI in some areas with no information (in the south of the Iberian Peninsula), but this effect is slightly different for each incidence angle, being the steepest angle (52.5°) the most affected. For the particular case of the Iberian Peninsula, this is a common effect, at least during the year 2018, the study period selected for this analysis. An RFI of about 9000 K located in Algeria could explain these data gaps (with a shape of RFI tails) on the Iberian Peninsula. The shape size of the affected area and the steepest angle (52.5°) being the most affected could indicate that the RFI originates from a directional antenna, pointing toward the horizon.

C. Analysis of High-Resolution SM Maps

Fig. 10 shows the histograms of the retrieved high-resolution SMOS SM at three incidence angles 32.5°, 42.5°, and 52.5°. Comparing the results for the three angles, it can be seen that the number of samples is smaller for 32.5° and 52.5° than for 42.5°. Taking this into consideration, the mean is similar for the three incidence angles, with a maximum value of 0.177 m^3/m^3 at 52.5° and a minimum value of 0.161 m^3/m^3 at 42.5°. The STD ranges from 0.097 m^3/m^3 at 52.5° to 0.112 m^3/m^3 at 32.5°. When the same analysis is carried out using the concurrent samples at the three incidence angles (not shown), the STD is 0.109, 0.098, and 0.09 m^3/m^3 at 32.5°, 42.5°, and 52.5°, respectively, and the differences between the means of the high-resolution SMOS SM at these angles never exceed 0.01 m^3/m^3. The agreement between the high-resolution SCA_V SM and REMEDHUS *in situ* time series is displayed in Fig. 11. The scatter plot shows that the results obtained are close to the 1:1 line and the estimates with the three SMOS incidence angles are consistent ($R \geq 0.57$, ubRMSE $\leq$ 0.077 m^3/m^3, |bias| $\leq$ 0.013 m^3/m^3, and p-value $\leq$ 0.01), although a larger number of samples would be necessary to confirm these results. Due to the missing synchronization between Sentinel-1, SMAP, and SMOS acquisition orbits (see Fig. 12), the number of samples is much lower at high resolution than at low resolution (see Figs. 6 and 11), which is a limiting factor considering the fast SM dynamics. To develop an operational version of the high-resolution SMOS SM, only simultaneously measurements from Sentinel-1 and SMOS will be required, which would improve the temporal resolution.

Fig. 13 shows the low- (top) and high-resolution (bottom) SMOS SM maps for January 3, 2018, both retrieved using the SCA_V with the parameters presented in Tables II and III. The high-resolution SMOS SM map at 52.5° is dryer than the maps at 32.5° and 42.5°. This effect can also be seen at low resolution, which means it is not introduced by the single-acquisition disaggregation technique. Differences in SM maps at individual incidence angles may be due to the fact that one constant set of ω and h_s parameters is obtained for the entire year of 2018. The result could potentially be improved by optimizing these parameters for shorter time periods, for example, per season, per months, or even fortnights.

V. Conclusion and Perspectives

In this study, the effective scattering albedo (ω) and soil roughness (h_s) described in the $\tau - \omega$ radiative transfer model have been calibrated independently for three SMOS incidence angles (32.5 $\pm$ 5°, 42.5 $\pm$ 5°, and 52.5 $\pm$ 5°), over the four main land covers (croplands, savannas, grassland, and shrublands) within the Iberian Peninsula, for the year 2018. These vegetation and soil parameters have been applied within the SCA at vertical polarization (SCA_V) to low-resolution (25-km grid) SMOS TB in order to estimate low-resolution SM maps that have been shown to be consistent among them (mean differences below 0.007 m^3/m^3) and show good agreement ($R \geq 0.75$ and ubRMSE $\leq$ 0.06 m^3/m^3) with 0–5 cm ground-based measurements from the REMEDHUS network. A single-pass active–passive disaggregation technique (3) has been applied, using the optimal ω and h_s values, to SMOS and Sentinel-1 data to estimate fine-scale (1 km) brightness temperatures at vertical polarization (TB_V) at the three respective incidence angles. Finally, the SCA_V is applied to obtain the high-resolution (1 km) SM maps for the Iberian Peninsula.

Regarding the incidence angle- and land cover-adapted parametrization of ω and h_s, results show (see Tables II and III) an increasing trend of the estimated ω with increasing SMOS incidence angle and an opposite trend for h_s. For the three SMOS incidence angles tested, the selection of optimal ω has a significant impact on the results, taking into consideration the R, the ubRMSE, and the bias. Instead, the optimal value of h_s does not affect the final result as much as ω (see Figs. 3 and 4). Scattering albedo has shown a very low variability with the land cover type, ranging from a minimum value of 0.02 at 32.5° to a maximum value of 0.12 at 52.5°. Soil roughness ranges from a minimum value of 0.01 at 52.5° to a maximum value of 0.18 at 32.5°, for four land cover types (savannas, croplands, grasslands, and shrublands).

The SCA_V algorithm has been applied to retrieve the low-resolution SM maps (25-km grid) using simultaneously the SMOS TB_V with the optimal values of ω and h_s. The resulting SM maps were validated against the REMEDHUS SM *in situ* measurements, using R, ubRMSE, and bias. Retrieved SM at the different incidence angles has revealed considerable agreement between them, being able to capture wet up and dry down events. The best statistical performance is obtained at 32.5° with a $R = 0.88$ and an ubRMSE = 0.05 m^3/m^3, while the worst is obtained at 52.5° with a $R = 0.75$ and an ubRMSE = 0.06 m^3/m^3. A dry bias is present for all three incidence angles. This mismatch between satellite estimations and *in situ* observations at REMEDHUS could be explained by the inherent scale gap when comparing a point-scale *in situ* measurement against an area-averaged satellite-based SM estimation. In addition, the underestimation of SM could be the result of underestimating the soil temperature (derived from the NASA GEOS-5 models), which leads to an overestimation of the soil microwave emissivity and, in turn, in an underestimation of SM.

The active–passive covariation parameter (β) is a crucial variable to disaggregate the SMOS TB_V (3) with the single-acquisition methodology applied in this study. In this way, β has been retrieved individually for the three SMOS incidence angles. This active–passive covariation has revealed a dependence with the Sentinel-1 incidence angle. The β values gradually decrease with the increase of the Sentinel-1 incidence angle (see Fig. 7). This effect is less evident for larger SMOS incidence angles (e.g., 52.5°). There is also a dependence of β with the SMOS incidence angle, the steeper the SMOS angle, the lower the covariation values, in magnitude. This means that it is less sensitive to changes in soil emissivity for higher SMOS incidence angles due to the stronger effect of vegetation during elongated ray path through the canopy.

The single-acquisition methodology allows us to merge active (Sentinel-1) and passive (SMOS) observations for disaggregating the coarse-resolution SMOS TB_V at $\theta = 32.5 \pm 5°$, 42.5 $\pm$ 5°, and 52.5 $\pm$ 5°, independently. Disaggregated SMOS TB_V (1 km), obtained using the estimated β, and optimal ω and h_s values (see Tables II and III), has been compared with the BEC SMOS Level 3 TB_V (12.5-km grid), across the Iberian Peninsula at 32.5°, 42.5°, and 52.5°, independently. Overall, TB_V maps show similar spatial distribution and temporal evolution between high and low resolution (see Figs. 8 and 9), for the three incidence angles studied. Slightly higher differences were found at 52.5°, but the mean difference never exceeds 0.38 K.

Finally, the SCA_V algorithm was applied to the disaggregated SMOS TB_V, retrieving high-resolution (1 km) SM maps at 32.5°, 42.5°, and 52.5°. A comparison of these high-resolution SM maps, across the Iberian Peninsula for 2018, exhibits similar patterns in their distributions, despite the differences in the number of samples for the different incidence angles. The mean difference between the three incidence angles was about 0.016 m^3/m^3. When analyzing daily SM maps, some differences can be observed in the retrievals of the same day among three incidence angles (see Fig. 13, bottom). These differences were not introduced by the single-acquisition disaggregation methodology because they were already present at low resolution (see Fig. 13, top). Disparities in retrieved SM maps at different incidence angles may be due to the fact that both ω and h_s parameters were optimized for the entire year of 2018 with a unique value, instead of considering shorter periods (e.g., seasonal or monthly) to derive variable ω and h_s values over time.

Results presented in this study are intended to underline the relevance of developing a land cover-specific and incidence angle-adaptive parametrization of radiative transfer models to accurately estimate SM from space-borne radiometers operating in low-frequency microwaves. In addition, we implement and tested further a single-pass method to downscale SMOS TB with Sentinel-1 backscatter for any individual incidence angle combination (radar and radiometer). This is especially relevant taking into account upcoming missions, such as CIMR, ROSE-L Copernicus high-priority missions, and Sentinel-1 next generation, which offer great potential to estimate high-resolution SM through the synergy of active and passive microwave sensors.

Acknowledgment

The authors would like to thank the Water Resources Research Group of the University of Salamanca, Villamayor, Spain, and Raul Díez García for their support and helpful comments. This work was supported with the MIT-Germany Seed Fund "Global Water Cycle and Environmental Monitoring using Active and Passive Satellite-Based Microwave Instruments."

References

[1] T. Schmugge, "Applications of passive microwave observations of surface soil moisture," *J. Hydrol.*, vols. 212–213, pp. 188–197, Dec. 1998, doi: 10.1016/S0022-1694(98)00209-1.

[2] Y. H. Kerr *et al.*, "The SMOS mission: New tool for monitoring key elements of the global water cycle," *Proc. IEEE*, vol. 98, no. 5, pp. 666–687, May 2010, doi: 10.1109/JPROC.2010.2043032.

[3] D. Entekhabi *et al.*, "The soil moisture active passive (SMAP) mission," *Proc. IEEE*, vol. 98, no. 5, pp. 704–716, May 2010, doi: 10.1109/JPROC.2010.2043918.

[4] T. J. Jackson and T. J. Schmugge, "Passive microwave remote sensing system for soil moisture: Some supporting research," *IEEE Trans. Geosci. Remote Sens.*, vol. 27, no. 2, pp. 225–235, Mar. 1989, doi: 10.1109/36.20301.

[5] J. Ballabrera-Poy *et al.*, "A new space technology for ocean observation: The SMOS mission," *Scientia Marina*, vol. 76, no. S1, pp. 249–259, Sep. 2012, doi: 10.3989/scimar.03621.19K.

[6] T. J. Jackson, "III. Measuring surface soil moisture using passive microwave remote sensing," *Hydrol. Processes*, vol. 7, no. 2, pp. 139–152, Apr. 1993, doi: 10.1002/hyp.3360070205.

[7] E. G. Njoku and L. Li, "Retrieval of land surface parameters using passive microwave measurements at 6–18 GHz," *IEEE Trans. Geosci. Remote Sens.*, vol. 37, no. 1, pp. 79–93, 1999, doi: 10.1109/36.739125.

[8] M. Owe, R. de Jeu, and J. Walker, "A methodology for surface soil moisture and vegetation optical depth retrieval using the microwave polarization difference index," *IEEE Trans. Geosci. Remote Sens.*, vol. 39, no. 8, pp. 1643–1654, Aug. 2001, doi: 10.1109/36.942542.

[9] A. G. Konings, M. Piles, K. Rötzer, K. A. McColl, S. K. Chan, and D. Entekhabi, "Vegetation optical depth and scattering albedo retrieval using time series of dual-polarized L-band radiometer observations," *Remote Sens. Environ.*, vol. 172, pp. 178–189, Jan. 2016, doi: 10.1016/j.rse.2015.11.009.

[10] R. Fernandez-Moran *et al.*, "SMOS-IC: An alternative SMOS soil moisture and vegetation optical depth product," *Remote Sens.*, vol. 9, no. 5, p. 457, May 2017, doi: 10.3390/rs9050457.

[11] P. E. O'Neill *et al.*, "SMAP L2 radiometer half-orbit 36 km EASE-grid soil moisture, version 8," NASA Nat. Snow Ice Data Center DAAC, Tech. Rep., 2021, doi: 10.5067/LPJ8F0TAK6E0. AQ:3

[12] A. F. Feldman, R. Akbar, and D. Entekhabi, "Characterization of higher-order scattering from vegetation with SMAP measurements," *Remote Sens. Environ.*, vol. 219, pp. 324–338, Dec. 2018, doi: 10.1016/j.rse.2018.10.022.

[13] T. Mo, B. J. Choudhury, T. J. Schmugge, J. R. Wang, and T. J. Jackson, "A model for microwave emission from vegetation-covered fields," *J. Geophys. Res.*, vol. 87, no. C13, p. 11229, 1982, doi: 10.1029/JC087iC13p11229.

[14] R. Van der Schalie, R. M. Parinussa, L. J. Renzullo, A. I. J. M. van Dijk, C.-H. Su, and R. A. M. de Jeu, "SMOS soil moisture retrievals using the land parameter retrieval model: Evaluation over the Murrumbidgee Catchment, southeast Australia," *Remote Sens. Environ.*, vol. 163, pp. 70–79, Jun. 2015.

[15] R. V. D. Schalie, Y. H. Kerr, J. P. Wigneron, N. J. Rodríguez-Fernández, A. Al-Yaari, and R. A. M. D. Jeu, "Global SMOS soil moisture retrievals from the land parameter retrieval model," *Int. J. Appl. Earth Observ. Geoinf.*, vol. 45, pp. 125–134, Mar. 2016, doi: 10.1016/j.jag.2015.08.005.

[16] R. Fernandez-Moran *et al.*, "A new calibration of the effective scattering albedo and soil roughness parameters in the SMOS SM retrieval algorithm," *Int. J. Appl. Earth Observ. Geoinform.*, vol. 62, pp. 27–38, Oct. 2017, doi: 10.1016/j.jag.2017.05.013.

[17] S. Peischl, J. P. Walker, N. Ye, D. Ryu, and Y. Kerr, "Sensitivity of multi-parameter soil moisture retrievals to incidence angle configuration," *Remote Sens. Environ.*, vol. 143, pp. 64–72, Mar. 2014, doi: 10.1016/j.rse.2013.11.019.

[18] L. Karthikeyan *et al.*, "Simultaneous retrieval of global scale vegetation optical depth, surface roughness, and soil moisture using X-band AMSR-E observations," *Remote Sens. Environ.*, vol. 234, Dec. 2019, Art. no. 111473, doi: 10.1016/j.rse.2019.111473.

[19] A. Camps, J. Gourrion, J. M. Tarongi, A. Gutierrez, J. Barbosa, and R. Castro, "RFI analysis in SMOS imagery," in *Proc. IEEE Int. Geosci. Remote Sens. Symp.*, Jul. 2010, pp. 2007–2010, doi: 10.1109/IGARSS.2010.5654268.

[20] M. Piles *et al.*, "A downscaling approach for SMOS land observations: Evaluation of high-resolution soil moisture maps over the Iberian peninsula," *IEEE J. Sel. Topics Appl. Earth Observ. Remote Sens.*, vol. 7, no. 9, pp. 3845–3857, Sep. 2014, doi: 10.1109/JSTARS.2014.2325398.

[21] G. Portal *et al.*, "A spatially consistent downscaling approach for SMOS using an adaptive moving window," *IEEE J. Sel. Topics Appl. Earth Observ. Remote Sens.*, vol. 11, no. 6, pp. 1883–1894, Jun. 2018, doi: 10.1109/JSTARS.2018.2832447.

[22] N. N. Das *et al.*, "The SMAP and Copernicus sentinel 1A/B microwave active-passive high resolution surface soil moisture product," *Remote Sens. Environ.*, vol. 233, Nov. 2019, Art. no. 111380, doi: 10.1016/j.rse.2019.111380.

[23] O. Merlin, M. J. Escorihuela, M. A. Mayoral, O. Hagolle, A. Al Bitar, and Y. Kerr, "Self-calibrated evaporation-based disaggregation of SMOS soil moisture: An evaluation study at 3 km and 100 m resolution in Catalunya, Spain," *Remote Sens. Environ.*, vol. 130, pp. 25–38, Mar. 2013, doi: 10.1016/j.rse.2012.11.008.

[24] N. Vergopolan *et al.*, "SMAP-HydroBlocks, a 30-m satellite-based soil moisture dataset for the conterminous U.S.," *Sci. Data*, vol. 8, no. 1, p. 264, Oct. 2021, doi: 10.1038/s41597-021-01050-2.

[25] H.-J.-F. Benninga, R. van der Velde, and Z. Su, "Sentinel-1 soil moisture content and its uncertainty over sparsely vegetated fields," *J. Hydrol. X*, vol. 9, Dec. 2020, Art. no. 100066, doi: 10.1016/j.hydroa.2020.100066.

[26] I. Zakharov *et al.*, "Retrieval of surface soil moisture from Sentinel-1 time series for reclamation of wetland sites," *IEEE J. Sel. Topics Appl. Earth Observ. Remote Sens.*, vol. 13, pp. 3569–3578, 2020, doi: 10.1109/JSTARS.2020.3004062.

[27] D. Palmisano, F. Mattia, A. Balenzano, G. Satalino, N. Pierdicca, and A. V. M. Guarnieri, "Sentinel-1 sensitivity to soil moisture at high incidence angle and the impact on retrieval over seasonal crops," *IEEE Trans. Geosci. Remote Sens.*, vol. 59, no. 9, pp. 7308–7321, Sep. 2021, doi: 10.1109/TGRS.2020.3033887.

[28] A. Balenzano *et al.*, "Sentinel-1 soil moisture at 1 km resolution: A validation study," *Remote Sens. Environ.*, vol. 263, Sep. 2021, Art. no. 112554, doi: 10.1016/j.rse.2021.112554.

[29] B. Bauer-Marschallinger *et al.*, "Toward global soil moisture monitoring with Sentinel-1: Harnessing assets and overcoming obstacles," *IEEE Trans. Geosci. Remote Sens.*, vol. 57, no. 1, pp. 520–539, Dec. 2019, doi: 10.1109/TGRS.2018.2858004.

[30] P. K. Srivastava, D. Han, M. R. Ramirez, and T. Islam, "Machine learning techniques for downscaling SMOS satellite soil moisture using MODIS land surface temperature for hydrological application," *Water Resour. Manage.*, vol. 27, no. 8, pp. 3127–3144, Jun. 2013, doi: 10.1007/s11269-013-0337-9.

[31] S. Chakrabarti, J. Judge, T. Bongiovanni, A. Rangarajan, and S. Ranka, "Disaggregation of remotely sensed soil moisture in heterogeneous landscapes using holistic structure-based models," *IEEE Trans. Geosci. Remote Sens.*, vol. 54, no. 8, pp. 4629–4641, Apr. 2016, doi: 10.1109/TGRS.2016.2547389.

[32] H. Jiang, H. Shen, H. Li, F. Lei, W. Gan, and L. Zhang, "Evaluation of multiple downscaled microwave soil moisture products over the central Tibetan Plateau," *Remote Sens.*, vol. 9, no. 5, p. 402, Apr. 2017, doi: 10.3390/rs9050402.

[33] J. F. Munoz-Martin, D. Llaveria, C. Herbert, M. Pablos, H. Park, and A. Camps, "Soil moisture estimation synergy using GNSS-R and L-band microwave radiometry data from FSSCat/FMPL-2," *Remote Sens.*, vol. 13, no. 5, p. 994, Mar. 2021, doi: 10.3390/rs13050994.

[34] O. Merlin, A. G. Chehbouni, Y. H. Kerr, E. G. Njoku, and D. Entekhabi, "A combined modeling and multispectral/multiresolution remote sensing approach for disaggregation of surface soil moisture: Application to SMOS configuration," *IEEE Trans. Geosci. Remote Sens.*, vol. 43, no. 9, pp. 2036–2050, Sep. 2005, doi: 10.1109/TGRS.2005.853192.

[35] M. Piles *et al.*, "Downscaling SMOS-derived soil moisture using MODIS visible/infrared data," *IEEE Trans. Geosci. Remote Sens.*, vol. 49, no. 9, pp. 3156–3166, Sep. 2011, doi: 10.1109/TGRS.2011.2120615.

[36] M. Piles, G. P. Petropoulos, N. Sánchez, Á. González-Zamora, and G. Ireland, "Towards improved spatio-temporal resolution soil moisture retrievals from the synergy of SMOS and MSG SEVIRI spaceborne observations," *Remote Sens. Environ.*, vol. 180, pp. 403–417, Jul. 2016, doi: 10.1016/j.rse.2016.02.048.

[37] M. Piles, D. Entekhabi, and A. Camps, "A change detection algorithm for retrieving high-resolution soil moisture from SMAP radar and radiometer observations," *IEEE Trans. Geosci. Remote Sens.*, vol. 47, no. 12, pp. 4125–4131, Dec. 2009, doi: 10.1109/TGRS.2009.2022088.

[38] N. N. Das, D. Entekhabi, and E. G. Njoku, "An algorithm for merging SMAP radiometer and radar data for high-resolution soil-moisture retrieval," *IEEE Trans. Geosci. Remote Sens.*, vol. 49, no. 5, pp. 1504–1512, May 2011, doi: 10.1109/TGRS.2010.2089526.

[39] J. Pellenq *et al.*, "A disaggregation scheme for soil moisture based on topography and soil depth," *J. Hydrol.*, vol. 276, no. 1, pp. 112–127, May 2003, doi: 10.1016/S0022-1694(03)00066-0.

[40] J. Peng, A. Loew, O. Merlin, and N. E. C. Verhoest, "A review of spatial downscaling of satellite remotely sensed soil moisture," *Rev. Geophys.*, vol. 55, no. 2, pp. 341–366, Jun. 2017, doi: 10.1002/2016RG000543.

[41] T. Jagdhuber *et al.*, "Estimation of active-passive microwave covariation using SMAP and Sentinel-1 data," *Remote Sens. Environ.*, vol. 225, pp. 458–468, May 2019, doi: 10.1016/j.rse.2019.03.021.

[42] M. Piles, K. A. McColl, D. Entekhabi, N. Das, and M. Pablos, "Sensitivity of aquarius active and passive measurements temporal covariability to land surface characteristics," *IEEE Trans. Geosci. Remote Sens.*, vol. 53, no. 8, pp. 4700–4711, Aug. 2015, doi: 10.1109/TGRS.2015.2407611.

[43] M. Martín-Neira *et al.*, "SMOS instrument performance and calibration after six years in orbit," *Remote Sens. Environ.*, vol. 180, pp. 19–39, Jul. 2016, doi: 10.1016/j.rse.2016.02.036.

[44] *La Moncloa. Geography of Spain [Spain/History and Culture/Geography]*. Accessed: Dec. 4, 2022. [Online]. Available: https://www.lamoncloa.gob.es/lang/en/espana/historyandculture/geography/Paginas/index.aspx

[45] *BEC FTP Service—BEC (Barcelona Expert Center)*. Accessed: Dec. 10, 2022. [Online]. Available: http://bec.icm.csic.es/bec-ftp-service/

[46] *Earthdata Search*. Accessed: Dec. 10, 2022. [Online]. Available: https://search.earthdata.nasa.gov/search

[47] *APPEEARS*. Accessed: Dec. 10, 2022. [Online]. Available: https://lpdaacsvc.cr.usgs.gov/appeears/

[48] *Climate Data Store*. Accessed: Dec. 10, 2022. [Online]. Available: https://cds.climate.copernicus.eu/cdsapp#!/dataset/reanalysis-era5-land?tab=form

[49] *International Soil Moisture Network*. Accessed: Jul. 27, 2021. [Online]. Available: https://www.geo.tuwien.ac.at/insitu/data_viewer/

[50] M. Pablos, C. González-Haro, and Y. M. Piles. (Dec. 19, 2020). *BEC SMOS Soil Moisture Products Description*. [Online]. Available: http://bec.icm.csic.es/doc/BEC_SMOS_PD_SM_L3v3_L4v5.pdf

[51] N. N. Das *et al.*, "SMAP/Sentinel-1 L2 radiometer/radar 30-second scene 3 km EASE-grid soil moisture, version 3," NASA Nat. Snow Ice Data Center DAAC, Tech. Rep., 2020, doi: 10.5067/ASB0EQO2LYJV.

[52] J. Muñoz-Sabater *et al.*, "ERA5-Land: A state-of-the-art global reanalysis dataset for land applications," *Earth Syst. Sci. Data*, vol. 13, pp. 1–50, Mar. 2021, doi: 10.5194/essd-2021-82.

[53] N. Sanchez, J. Martinez-Fernandez, A. Scaini, and C. Perez-Gutierrez, "Validation of the SMOS L2 soil moisture data in the REMEDHUS network (Spain)," *IEEE Trans. Geosci. Remote Sens.*, vol. 50, no. 5, pp. 1602–1611, May 2012, doi: 10.1109/TGRS.2012.2186971.

[54] W. A. Dorigo *et al.*, "The international soil moisture network: A data hosting facility for global *in situ* soil moisture measurements," *Hydrol. Earth Syst. Sci.*, vol. 15, no. 5, pp. 1675–1698, May 2011, doi: 10.5194/hess-15-1675-2011.

[55] D. Sulla-Menashe and M. A. Friedl, "User guide to collection 6 MODIS land cover (MCD12Q1 and MCD12C1) product," Tech. Rep., 2018, p. 18. AQ:4

[56] *The IGBP-DIS Global 1 km Land Cover Data Set, DISCover: First Results*. Accessed: Jul. 27, 2021. [Online]. Available: https://pubs.er.usgs.gov/publication/70187679

[57] R. H. Reichle *et al.*, "SMAP L4 global 9 km EASE-grid surface and root zone soil moisture land model constants, version 5," NASA Nat. Snow Ice Data Center DAAC, Tech. Rep., 2020, doi: 10.5067/5C36BVQZW28K.

[58] M. Piles, M. Vall-llossera, A. Camps, M. Talone, and A. Monerris, "Analysis of a least-squares soil moisture retrieval algorithm from L-band passive observations," *Remote Sens.*, vol. 2, no. 1, pp. 352–374, Jan. 2010, doi: 10.3390/rs2010352.

[59] G. Portal, M. Vall-llossera, T. Jagdhuber, A. Camps, M. Pablos', and M. Piles, "Incidence angle diversity on L-Band microwave radiometry and its impact on consistent soil moisture retrievals," in *Proc. IEEE Int. Geosci. Remote Sens. Symp. (IGARSS)*, Jul. 2021, pp. 6186–6189, doi: 10.1109/IGARSS47720.2021.9553132.

[60] P. O'Neill *et al.*, "Algorithm theoretical basis document. Level 2 & 3 soil moisture (passive) data products," Tech. Rep., 2018, p. 111.

[61] M. Kurum, "Quantifying scattering albedo in microwave emission of vegetated terrain," *Remote Sens. Environ.*, vol. 129, pp. 66–74, Feb. 2013, doi: 10.1016/j.rse.2015.02.015.

[62] J.-P. Wigneron, L. Laguerre, and Y. H. Kerr, "A simple parameterization of the L-band microwave emission from rough agricultural soils," *IEEE Trans. Geosci. Remote Sens.*, vol. 39, no. 8, pp. 1697–1707, 2001, doi: 10.1109/36.942548.

[63] J.-P. Wigneron *et al.*, "L-band microwave emission of the biosphere (L-MEB) model: Description and calibration against experimental data sets over crop fields," *Remote Sens. Environ.*, vol. 107, no. 4, pp. 639–655, Apr. 2007, doi: 10.1016/j.rse.2006.10.014.

[64] V. L. Mironov, L. G. Kosolapova, and S. V. Fomin, "Physically and mineralogically based spectroscopic dielectric model for moist soils," *IEEE Trans. Geosci. Remote Sens.*, vol. 47, no. 7, pp. 2059–2070, Jul. 2009, doi: 10.1109/TGRS.2008.2011631.

[65] D. Entekhabi, R. H. Reichle, R. D. Koster, and W. T. Crow, "Performance metrics for soil moisture retrievals and application requirements," *J. Hydrometeorol.*, vol. 11, no. 3, pp. 832–840, Jun. 2010, doi: 10.1175/2010JHM1223.1.

[66] G. Portal *et al.*, "Assessment of multi-scale SMOS and SMAP soil moisture products across the Iberian Peninsula," *Remote Sens.*, vol. 12, no. 3, p. 570, Feb. 2020, doi: 10.3390/rs12030570.

[67] M. Pablos, J. Martínez-Fernández, M. Piles, N. Sánchez, M. Vall-llossera, and Y. A. Camps, "Multi-temporal evaluation of soil moisture and land surface temperature dynamics using *in situ* and satellite observations," Tech. Rep., Jul. 2016, doi: 10.13039/100007406.

[68] T. Jagdhuber *et al.*, "Physics-based modeling of active-passive microwave covariations for geophysical retrievals," in *Proc. IEEE Int. Geosci. Remote Sens. Symp. (IGARSS)*, Jul. 2018, pp. 250–253, doi: 10.1109/IGARSS.2018.8518975.

[69] J.-P. Wigneron *et al.*, "Modelling the passive microwave signature from land surfaces: A review of recent results and application to the L-band SMOS & SMAP soil moisture retrieval algorithms," *Remote Sens. Environ.*, vol. 192, pp. 238–262, Apr. 2017, doi: 10.1016/j.rse.2017.01.024.

[70] *The SMOS Soil Moisture Retrieval Algorithm*. Accessed: Aug. 14, 2021. [Online]. Available: https://ieeexplore.ieee.org/document/6161633

[71] C. Cui *et al.*, "Soil moisture mapping from satellites: An intercomparison of SMAP, SMOS, FY3B, AMSR2, and ESA CCI over two dense network regions at different spatial scales," *Remote Sens.*, vol. 10, no. 2, p. 33, Dec. 2017, doi: 10.3390/rs10010033.

[72] Y. Chen *et al.*, "Evaluation of SMAP, SMOS, and AMSR2 soil moisture retrievals against observations from two networks on the Tibetan Plateau," *J. Geophys. Research: Atmos.*, vol. 122, no. 11, pp. 5780–5792, Jun. 2017, doi: 10.1002/2016JD026388.

[73] *Multi-Frequency Estimation of Canopy Penetration Depths from SMAP/AMSR2 Radiometer and Icesat LiDAR Data*. Accessed: Aug. 16, 2021. [Online]. Available: https://ieeexplore.ieee.org/document/8517438

[74] A. Camps, M. Vall-llossera, N. Duffo, F. Torres, and I. Corbella, "Performance of sea surface salinity and soil moisture retrieval algorithms with different auxiliary datasets in 2-D L-band aperture synthesis interferometric radiometers," *IEEE Trans. Geosci. Remote Sens.*, vol. 43, no. 5, pp. 1189–1200, May 2005, doi: 10.1109/TGRS.2004.842096.

Gerard Portal (Member, IEEE) was born in Barcelona, Spain, in 1988. He received the Telecommunication Engineering and Ph.D. degrees in the program of signal theory and communications from the Polytechnic University of Catalonia (UPC), Barcelona, in 2015 and 2022, respectively.

In September 2016, he joined the Department of Signal Theory and Communications, UPC. He has been involved in the development and improvement of soil moisture disaggregation algorithms, as well as in the analysis of passive and active microwave parameters. His research interests include both active and passive remote sensing, as well as the development of downscaling algorithm applying synergies of data from different sensors (optical, thermal, and at microwave frequencies).

Mercè Vall-llossera (Senior Member, IEEE) was born in Lleida, Spain. She received the Telecommunications Engineer and Ph.D. degrees in telecommunications engineering from the Universitat Politècnica de Catalunya (UPC), Barcelona, Spain, in 1990 and 1994, respectively.

Since November 1990, she has been teaching at Escuela Técnica Superior de Ingeniería de Telecomunicaciones de Barcelona (ETSETB, UPC). During the Ph.D., she was working in numerical methods applied to radar target characterization and antenna design. She applied high-frequency approximations to radar analysis and graphical processing for parabolic antenna design. In 1998, with the rest of the multiband fractal received first prize of the European Information and Technology Prize. Since 1998, her research has been devoted to passive remote sensing, working in the Earth Explorer mission European Spatial Agency (ESA) Soil Moisture and Ocean Salinity (SMOS) with the Passive RSLab team within the frame of several contracts with the ESA), directly or as subcontractors of some enterprises (EADS-Casa Espacio, Deimos Engiheria). Her researching experience involves, interferometric radiometry, SMOS retrieval, downscaling algorithm for spatial resolution improvement, and added-value products from SMOS, AQUARIUS, and Soil Moisture Active Passive (SMAP) missions. Nowadays, she is interested in L-Band Soil Moisture and VOD new applications, such as drought detection, pest and plagues monitoring, crop yield and biomass estimations, and forest fires prevention.

Dr. Vall-llossera is a Senior Member of the IEEE Society and she is a Regular Reviewer of the IEEE TRANSACTIONS ON GEOSCIENCE AND REMOTE SENSING (IEEE TGRS), *Journal of Hydrology*, *Remote Sensing of Environment*, the IEEE JOURNAL OF SELECTED TOPICS IN APPLIED EARTH OBSERVATIONS AND REMOTE SENSING, IEEE GEOSCIENCE AND REMOTE SENSING LETTERS, IGARSS, *Journal of Earth System Science*, *Journal of Hydrometeorology*, and *Water Resources Research*. In 2007, she participated in the organization of the International Geoscience and Remote Sensing Symposium (IGARSS'07).

María Piles (Senior Member, IEEE) received the B.Sc. degree in telecommunication engineering from the Universitat Politècnica de València, València, Spain, in 2005, and the Ph.D. degree in signal theory and communications from the Universitat Politècnica de Catalunya (UPC), Barcelona, Spain, in 2010.

She was a Research Fellow with The University of Melbourne, Melbourne, VIC, Australia, in 2010, and a Research Scientist with UPC from 2011 to 2016, associated with the Massachusetts Institute of Technology, Cambridge, MA, USA. In 2016, she joined the Institute of Marine Sciences from the Spanish National Research Council, as a Research Scientist. Since 2017, she has been a Ramón y Cajal Senior Researcher with the Imaging Processing Laboratory, Universitat de València, València, Spain. She has published more than 70 articles (>3300 cites) in international peer-reviewed journals, four book chapters, and more than 100 international conference papers. Her research activity is centered in remote sensing for Earth observation, with special emphasis in microwave radiometers, radars, and hyperspectral sensors. She has wide experience in the retrieval of the water content in soils and vegetation from low-frequency microwaves and the development of multisensor techniques for enhanced retrievals with focus on agriculture, forestry, wildfire prevention, detection of extremes, and climate studies. She is actively involved within the scientific activities of the European Spatial Agency's (ESA) Soil Moisture and Ocean Salinity (SMOS) and the National Aeronautics and Space Administration's (NASA) Soil Moisture Active Passive (SMAP) missions, and she is a member of the Mission Advisory Group of the Copernicus Imaging Microwave Radiometer (CIMR, https://cimr.eu).

Thomas Jagdhuber (Senior Member, IEEE) received the Diploma degree in physical geography, physics, remote sensing, and geoinformatics from the Ludwig Maximilian University of Munich (LMU), Munich, Germany, and the Technical University (TUM) of Munich, Munich, in 2006, and the Ph.D. degree in hydrology from the Faculty of Science, University of Potsdam, Potsdam, Germany, in 2012.

Since 2007, he has been with the Microwaves and Radar Institute (HR), German Aerospace Center (DLR), Weßling, Germany, and since 2022, he leads the signatures research group of HR. From 2014 to 2019 and in 2022, he was a Yearly Visiting Scientist with the Massachusetts Institute of Technology (MIT), Boston, MA, USA, contributing to the preparation and continuation of the Soil Moisture Active Passive (SMAP) and SMAP/Sentinel-1 missions. He is also a Lecturer with the University of Jena, Jena, Germany, and the University of Augsburg, Augsburg, Germany. His main research interests include physics-based multisensor data integration with a focus on active and passive microwave interaction theory and polarimetric techniques for hydrological, agricultural, ecological, and cryospheric parameter modeling and estimation.

Dr. Jagdhuber was honored with the DLR Science Award for his research on polarimetric SAR decomposition techniques in 2014. Together with Prof. Entekhabi (MIT), he was awarded the MIT-MISTI Grant for global water cycle and environmental monitoring using active and passive satellite-based microwave instruments. He also serves as a reviewer for several international journals and conference boards.

Adriano Camps (Fellow, IEEE) joined the Electromagnetics and Photonics Engineering Group, Department of Signal Theory and Communications, Universitat Politècnica de Catalunya (UPC), as an Assistant Professor, in 1993, an Associate Professor in 1997, and a Full Professor since 2007. In 1999, he was on sabbatical leave with the Microwave Remote Sensing Laboratory, University of Massachusetts at Amherst, Amherst, MA, USA. His publication record includes over 245 articles in peer-reviewed journals, nine book chapters, and the book by Emery and Camps "*Introduction to Satellite Remote Sensing: Atmosphere, Ocean, Land and Cryosphere Applications*," (Elsevier, 2017), and more than 485 conference presentations. According to Google Scholar/Scopus, his H-index is 58/45, and his publications have received more than 13 242/9149 citations, and he has advised 27 Ph.D. thesis students (more than eight on-going) and more than 140 final projects and M.Eng. theses.

Dr. Camps has received several awards, among which the European Young Investigator Award in 2004, the Catalan Institution for Research and Advanced Studies (ICREA) Academia Research Award in 2009 and 2015, and the Duran Farell Award for Technology Transfer in 2000 and 2010 and the 2021 IEEE GRSS Education Award.

Miriam Pablos (Member, IEEE) received the B.Sc. degree in telecommunications engineering and the Ph.D. degree in signal theory and communications from the Technical University of Catalonia (UPC), Barcelona, Spain, in 2010 and 2016, respectively.

In 2009, she joined the Department of Signal Theory and Communications, UPC, where she was dedicated to the calibration and stability analysis of the Soil Moisture and Ocean Salinity (SMOS) radiometer. In 2011, she worked on a THz imaging security application, using interferometric radiometers at near field. From 2012 to 2016, she joined the Barcelona Expert Center (BEC) on Remote Sensing. She was mainly dedicated to analyze both brightness temperature and soil moisture at L-band from SMOS, Aquarius, and Soil Moisture Active Passive (SMAP) missions. Additionally, she was a Visiting Ph.D. Student with the Department of Civil and Environmental Engineering, Massachusetts Institute of Technology (MIT), Cambridge, MA, USA, from April 2015 to June 2015. She assessed passive and active microwave vegetation parameters and applied the multitemporal dual channel algorithm (MT-DCA) to airborne data to retrieve soil moisture. From 2017 to 2018, she was a Post-Doctoral Researcher with the Instituto Hispanoluso de Investigaciones Agrarias, University of Salamanca (USAL), Villamayor, Spain. She assessed agricultural drought indices over semiarid regions and helped in the maintenance of the Soil Moisture Measurements Stations Network of USAL (REMEDHUS), a cal/val site of SMOS and SMAP. Since 2018, she is with the Spanish National Research Council (CSIC) and become a member of the BEC again. She has been working on the improvement of the soil moisture disaggregation algorithm using microwave and optical data, in close collaboration with UPC. From September 2021 to December 2021, she was with the Technical University of Vienna (TU-Wien), Vienna, Austria, analyzing the behavior of active and passive microwave data over very dry regions. She has currently authored 18 international journal articles and over 25 conference proceedings. Her research interests include, but are not limited to, soil moisture retrieval algorithms, validation of satellite soil moisture products, and the development of added-value products and applications based on soil moisture.

Carlos López-Martínez (Senior Member, IEEE) received the M.Sc. degree in electrical engineering and the Ph.D. degree in remote sensing from the Universitat Politècnica de Catalunya (UPC), Barcelona, Spain, in 1999 and 2003, respectively, and the Postgraduate Diploma degree in data science and big data from the Universitat de Barcelona, Barcelona, in 2021.

He is currently an Associate Professor in the area of remote sensing and microwave technology with UPC. He has a large professional international experience at the German Aerospace Center (DLR), Germany, at the University of Rennes 1, Rennes, France, and as the Group Leader of the Remote Sensing and Natural Resources Modelling Team, Luxembourg Institute of Science and Technology, Esch-sur-Alzette, Luxembourg. He has broad academic teaching experience from bachelor's, master's, and Ph.D. levels to advanced technical tutorials presented at international conferences and space and research institutions worldwide. He has authored more than 200 articles in journals, books, and conference proceedings. His research interests include synthetic aperture radar (SAR) theory, statistics and applications, multidimensional SAR, radar polarimetry, physical parameter inversion, advanced digital signal processing, estimation theory, and harmonic analysis.

Dr. López-Martínez was a recipient of the EUSAR 2002 Conference Student Prize Paper Award, the EUSAR 2012 Conference First Place Student Paper Award, as a Coauthor, and the IEEE-GRSS 2013 GOLD Early Career Award. He has collaborated in the Spanish PAZ and the European Spatial Agency's (ESA) SAOCOM-CS missions and in the proposal of the Parsifal mission. He is a member of the ESA's Sentinel ROSE-L Mission Advisory Group. He was appointed the Vice-President of the IEEE-GRSS Spanish Chapter, and in 2016, he became its a Secretary and a Treasurer. Since 2011, he has been collaborating with the IEEE-GRSS Globalization initiative in Latin America, contributing to the creation of the IEEE-GRSS Chilean Chapter and the organization of the 2020 LAGIRSS conference, being appointed as Latin America liaison in 2019. He is also the Co-Chair of the Tutorial Technical Committee of the Indian 2020 and 2021 InGARSS conferences. He is an Associate Editor for the IEEE JOURNAL OF SELECTED TOPICS IN APPLIED EARTH OBSERVATIONS AND REMOTE SENSING and *Remote Sensing* (MDPI), acting also as an invited guest editor for several special issues.

Narendra N. Das was born in Bhilai, India. AQ:5
He received the B.E. degree in chemical engineering from the National Institute of Technology Raipur (formerly, Government Engineering College, Raipur), Raipur, India, and the master's and the Ph.D. degrees in biological and agricultural engineering from Texas A&M University, College Station, TX, USA, in 2005 and 2008, respectively.

In November 2020, he joined the Michigan State University (MSU), East Lansing, MI, USA, where he is currently an Associate Professor with the Department of Biosystems and Agricultural Engineering and the Department of Civil and Environmental Engineering. Prior to joining MSU, he was a Research Scientist with the NASA Jet Propulsion Laboratory (JPL), California Institute of Technology, Pasadena, CA, USA, for 12 years (2008–2020). In 2008, he joined JPL and conducted research in hydrology and microwave remote sensing, especially for soil moisture retrievals using the combination of radiometer and radar and the applications of soil moisture for weather, agriculture, and drought.

Dr. Das is a Science Team Member of the Soil Moisture Active and Passive (SMAP) mission. He is a Principal Investigator (PI) of the Applied Science NASA SERVIR Program to implement Drought and Crop Forecast System for East Africa region and Lower Mekong Basin countries. He is a Science Team Member of the NASA ISRO SAR (NISAR) mission with the responsibility to produce very high-resolution global soil moisture data product. He is also a PI of NASA Terrestrial Hydrology Program.

Dara Entekhabi (Fellow, IEEE) received the B.S. and M.S. degrees in geography from Clark University, Worcester, MA, USA, in 1983, 1985, and 1988, respectively, and the Ph.D. degree in civil and environmental engineering from the Massachusetts Institute of Technology (MIT), Cambridge, MA, in 1990.

He is currently a Professor with the Department of Civil and Environmental Engineering and the Department of Earth, Atmospheric and Planetary Sciences, MIT. He is the Science Team Lead of the National Aeronautics and Space Administration's Soil Moisture Active and Passive (SMAP) mission that was launched in January 2015. His research interests include terrestrial remote sensing, data assimilation, and coupled land-atmosphere systems modeling.

Prof. Entekhabi is also a fellow of the American Meteorological Society and the American Geophysical Union. He is a member of the National Academy of Engineering.